Åbo Akademi University

Simon Sandén

Recombination of Injected and Photogenerated Charge Carriers in Photovoltaic Blends and Devices

Recombination of Injected and Photogenerated Charge Carriers in Photovoltaic Blends and Devices

Simon Sandén

Physics
Center for Functional Materials
Faculty of Science and Engineering
Åbo Akademi University
Åbo, Finland, 2018

Supervisor
Professor Ronald Österbacka
Åbo Akademi University

Pre-Examiners
Professor Ana Flávia Nogueira
University of Campinas

Associate Professor Attila Mozer
University of Wollongong

Opponent for the public defense
Professor Fengling Zhang
Linköping University

ISBN 978-952-12-3666-2
Painosalama Oy – Åbo, Finland 2018

Table of Contents

Preface

The work in this thesis was performed under the supervision of Professor Ronald Österbacka at Physics, Faculty of Science and Engineering at Åbo Akademi University within the Center for Functional Materials. The work was partially founded, through different projects by the Academy of Finland as well as by grants given by Svenska tekniska vetenskapsakdemin i Finland, Tekniikan edistämissäätiö, the Magnus Ehrnrooth foundation, the Waldemar von Frenckell foundation, the Fortum foundation and the Scandinavia-Japan Sasakawa foundation.

My work as a researcher started in December 2006 when Ronald gave me the opportunity to participate in an industry project concerning the use of inorganic semiconductor nanoparticles in electronic devices. This project evolved into my Master's thesis work which I finished in 2008. Thereafter I was given the opportunity to pursue a Ph.D. in the study of organic solar cells, which I gladly accepted. I would like to thank Ronald for all the advice, suggestions and help during this long process.

Research is a collaborative process involving all members in the Organic Electronics group. I am especially grateful for my collaboration with Mathias Nyman, Oskar Sandberg and Nora Wilson as well as Harri Aarnio. As an experimentalist, I would like to thank our laboratory engineer Kjell-Mikael Källman, without whom no experiments could be done.

The research into organic solar cells has been thoroughly interdisciplinary with an especially intense and rewarding collaboration with the Laboratory of Physical Chemistry. I am particularly grateful to have had the opportunity to collaborate with Adjunct Professor Jan-Henrik Smått and fellow Ph. D. student Björn Törngren and Dr. Qian Xu as well as the other personnel and students at the Laboratory of Physical Chemistry.

As part of my Ph.D. studies I was given the opportunity to spend a year as a visiting researcher at the Research Center for Advanced Science and Technology at The University of Tokyo in Japan at the Segawa Laboratory. I am very grateful to Professor Segawa for inviting me to stay at his laboratory and would like to express a sincere thank you to Professor Kubo, with whom I did most of my research in Japan. In addition to this I would like to thank fellow Ph. D. student Akitsu who showed me some great restaurants around Tokyo as well as our research collaboration.

Last but not least I would like to thank all of my friends and especially my family for their support.

Simon Sandén
Åbo, 18.12.2018

List of Publications

This thesis is based on the five publications listed below:

I. Effect of a Large Hole Reservoir on the Charge Transport in TiO_2/Organic Hybrid Devices.
S. Sandén, O. Sandberg, Q. Xu, J.-H. Smått, G. Juška, M. Lindén and R. Österbacka
Physical Chemistry Chemical Physics **14**, 14186 (2012)
© 2012 The Royal Society of Chemistry

II. Influence of Equilibrium Charge Reservoir Formation on Photo Generated Charge Transport in TiO_2/Organic Devices.
S. Sandén, O. J. Sandberg, Q. Xu, J.-H. Smått, G. Juška, M. Lindén and R. Österbacka
Organic Electronics **15**, 3506 (2014) © 2014 Elsevier B. V.

III. Characterization of the Dominating Bulk Recombination in Bulk-Heterojunction Blends Using Photoinduced Absorption.
S. Sandén, N. M. Wilson, O. J. Sandberg and R. Österbacka
Applied Physics Letters **108**, 193301 (2016) © 2016 AIP Publishing

IV. Characterization of Recombination in P3HT:fullerene Blends: Clarifying the Influence of Interfacial States.
S. Sandén, N. M. Wilson, M. Nyman and R. Österbacka
Organic Electronics **42**, 131 (2017) © 2016 Elsevier B. V.

V. Generation of Photoexcitations and Trap-Assisted Recombination in TQ1:$PC_{71}BM$ Blends.
S. Sandén, N. M. Wilson, E. Wang and R. Österbacka
The Journal of Physical Chemistry C **121**, 8211 (2017)
© 2017 American Chemical Society

Author's Contribution

I. The author did all of the experimental work apart from the TiO_2 fabrication, wrote the first draft of the manuscript and finalized it together with the co-authors.

II. The author did all of the experimental work except for the TiO_2 fabrication, analyzed the data together with O. J. Sandberg and wrote the first draft of the manuscript and finalized it together with the co-authors.

III. The author did all of the experimental work, analyzed the data together with N. M. Wilson and O. J. Sandberg, wrote the first draft of the manuscript and finalized it together with the co-authors.

IV. The author did all of the experimental work, apart from the photo-CELIV measurement, analyzed the data together with N. M. Wilson and M. Nyman, wrote the first draft of the manuscript and finalized it together with the co-authors.

V. The author planned all the experiments and performed all of the experimental work, analyzed the data together with N. M. Wilson, wrote the first draft of the manuscript and finalized it together with the co-authors.

List of Additional Publications

1. Investigation of Plasmonic Gold-Silica Core-Shell Nanoparticle Stability in Dye-Sensitized Solar Cell Applications.
   B. Törngren, K. Akitsu, A. Ylinen, S. Sandén, H. Jiang, J. Ruokolainen, M. Komatsu, T. Hamamura, J. Nakazaki, T. Kubo, H. Segawa, R. Österbacka and J.-H. Smått
   Journal of Colloid and Interface Science **427**, 54 (2014)

2. Trap-Assisted Recombination via Integer Charge Transfer States in Organic Bulk Heterojunction Photovoltaics.
   Q. Bao, O. Sandberg, D. Dagnelund, S. Sandén, S. Braun, H. Aarnio, X. Liu, W. M. Chen, R. Österbacka and M. Fahlman
   Advanced Functional Materials **24**, 6309 (2014)

3. Plasmon Enhanced Polymer Sensitized Solar Cells.
   S. Sandén, K. Akitsu, B. Törngren, A. Ylinen, J.-H. Smått, T. Kubo, M. Matsumura, N. Otani, H. Segawa and R. Österbacka
   The Journal of Physical Chemistry C **119**, 5570 (2015)

4. Influence of TiO_2 Compact Layer Precursor on the Performance of Perovskite Solar Cells.
   P. Vivo, A. Ojanperä, J.-H. Smått, S. Sandén, S. G. Hashmi, K. Kaunisto, P. Ihalainen, M. T. Masood, R. Österbacka, P. D. Lund and H. Lemmetyinen
   Organic Electronics **41**, 287 (2017)

5. Determination of Surface Recombination Velocities at Contacts in Organic Semiconductor Devices Using Injected Carrier Reservoirs.
   O. J. Sandberg, S. Sandén, A. Sundqvist, J.-H. Smått and R. Österbacka
   Physical Review Letters **118**, 076601 (2017)

6. Method for Characterizing Bulk Recombination Using Photoinduced Absorption.
   N. M. Wilson, S. Sandén, O. J. Sandberg and R. Österbacka
   Journal of Applied Physics **121**, 095701 (2017)

7. On the Validity of MIS-CELIV for Mobility Determination in Organic Thin-Film Devices.
O. J. Sandberg, M. Nyman, S. Dahlström, S. Sandén, B. Törngren, J.-H. Smått and R. Österbacka
Applied Physics Letters **110**, 153504 (2017)

8. Impact of Film Thickness of Ultrathin Dip-Coated Compact TiO_2 Layers on the Performance of Mesoscopic Perovskite Solar Cells.
M. T. Masood, C. Weinberger, J. Sarfraz, E. Rosqvist, S. Sandén, O. J. Sandberg, P. Vivo, G. Hashmi, P. D. Lund, R. Österbacka and J.-H. Smått
ACS Applied Materials and Interfaces **9**, 17906 (2017)

9. Roll-to-Roll Manufacturing of Disposable Surface-Enhanced Raman Scattering (SERS) Sensors on Paper Based Substrates.
J. J. Saarinen, D. Valtakari, S. Sandén, J. Haapanen, T. Salminen, J. M. Mäkinen and J. Uozumi
Nordic Pulp and Paper Research Journal **32**, 222 (2017)

10. Minimizing structural deformation of gold nanorods in plasmon-enhanced dye-sensitized solar cells
B. Törngren, S. Sandén, J. O. Nyman, A. Tiihonen, H. Jiang, J. Ruokolainen, J. Halme, R. Österbacka and J.-H. Smått
Journal of Nanoparticle Reserch **19**, 365 (2017)

1. Introduction

Energy production is an important part of our global society and as nations are increasing their energy demand, improvements in the production and storage of energy will be a vital part of future research. A large part of the current energy production comes from fossil fuels which emit greenhouse gases, such as carbon dioxide (CO_2), which contribute to global warming. The development and implementation of technologies which are carbon neutral or have zero carbon emission will be an important issue in the near future.

Generation of electricity using solar energy has increased in the last few decades and is expected to expand in the near future [1]. Solar energy technologies can be divided into two categories: solar thermal and solar photovoltaics. Solar thermal energy production uses sunlight to heat water which drives a turbine to generate electricity. Solar photovoltaics, also called solar cells, on the other hand utilize the photovoltaic effect, where absorption of photons in a material leads to the production of an electrical current.

The first practical solar cell was developed by Bell Labs in 1954 having an efficiency around 6% [2]. Solar cells were first used in space applications [3,4] and they continue to be used in satellites, space probes and on the International Space Station [5]. During the last few decades, the cost of solar panels (an array of solar cells) has dropped significantly leading to an increase in the installation of solar panels on residential and commercial buildings [1,6].

Inorganic materials such as silicon, gallium arsenide and copper indium gallium selenide are typically used as the active material in solar cells. Drawbacks with the use of these kinds of materials are the high initial cost in energy when producing solar cells, their weight and the fact that they are brittle. The use of organic materials such as polymers and small molecules in solar cells are under intense research presently [7,8]. The advantages of organic materials are their solution processability and the possibility to modify their material properties by varying their chemical structure and composition [9]. Solar cells made from organic materials, i.e. organic solar cells, have reached efficiencies above 11% [10], making them appealing for use in commercial applications. There are still some drawbacks with organic materials, such as low stability in ambient conditions, which make encapsulation necessary to prevent degradation [11].

1.1. Organic Solar Cells

The active material in an organic solar cell typically consists of two components: an electron donating (donor) and accepting material (acceptor). One of the first types of organic solar cells utilized a donor and acceptor in a bilayer configuration which was sandwiched between an anode and a cathode, resulting in an efficiency around 1% [12]. The cause of the low efficiency was the fact that the initially formed photoexcitation in organic materials is a tightly bound electron-hole pair, called an exciton. The exciton has a high binding energy (0.1-0.5 eV) [13–15] compared to the available thermal energy at room temperature (0.026 eV). To split the exciton into a free electron and hole the difference in energy between the lowest unoccupied molecular orbital (LUMO) of the acceptor and the highest occupied molecular orbital (HOMO) of the donor needs to be larger than the exciton-binding energy [16]. In addition to the energy difference, the exciton must reach a donor/acceptor interface, where splitting into a free electron and hole can occur. Since the exciton diffusion length is typically around 10 nm in organic materials [17,18] and typical thicknesses of organic solar cells are around 100 nm, only a small number of excitons generated in bilayer solar cells will lead to the formation of free charges. To overcome the issue of a short exciton diffusion length, the bulk-heterojunction (BHJ) concept was developed [19,20]. In a BHJ, the donor and acceptor are blended together to form an interpenetrating network, where the domain size of each component is around 10-20 nm [21], thus excitons generated in the donor and acceptor are able to reach a donor/acceptor interface and split into free electrons and holes. A bulk-heterojunction solar cell is formed by sandwiching the BHJ blend between an anode and a (transparent) cathode, as shown schematically Figure 1.1a. To prevent hole (electron) extraction at the cathode (anode) an electron transport layer (ETL) and a hole transport layer (HTL) can be inserted between the cathode and anode, respectively. The relative energy levels of the different layers used in organic solar cells is shown in Figure 1.1b

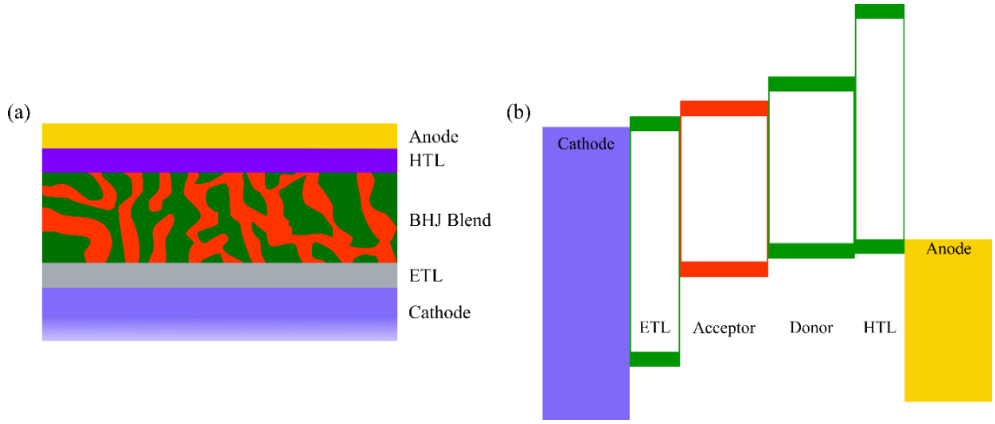

Figure 1.1. Schematic illustration of (a) a bulk-heterojunction solar cell showing a (transparent) cathode, the electron transport layer (ETL), the BHJ blend, a hole transport layer (HTL) and the anode and (b) the relative energy levels of the layers in an organic solar cell.

1.2. Efficiency of Solar Cells

The efficiency of a solar cell depends on a variety of factors, such as: how many photons are absorbed, the conversion efficiency of an absorbed photon into free charges, how efficiently charges are transported to and extracted at the contacts. Furthermore, recombination of charges inside the device before extraction will also limit the efficiency [22]. The absorption coefficient determines the thickness needed to absorb most light in solar cells. Organic materials typically have a relatively high absorption coefficient, so that solar cells need a thickness between 100 and 200 nm to absorb the majority of incoming light. The absorption spectrum of solar cell materials should also match the Sun's emission spectrum. A standard spectrum called AM 1.5 is typically used to characterize solar cells. The AM 1.5 spectrum corresponds to the solar irradiation at the surface of the Earth when the Sun's angle, relative to zenith, is 48° [23]. The AM 1.5 solar spectrum is shown in Figure 1.2 along with the absorption spectrum of two conjugated polymers: P3HT and TQ1 and a donor material: the fullerene derivative $PC_{71}BM$. Materials with lower bandgaps can absorb light at longer wavelengths. Thus, a larger part of the solar spectrum can be absorbed and more photons are absorbed leading to more efficient solar cells. Efficient exciton dissociation can be achieved by controlling the morphology of the BHJ blend, ensuring that most excitons can

reach the donor/acceptor interface [24]. The transport of free charges depends on the mobility of the charge carriers and by having an interpenetrating morphology efficient transport to the contacts can be ensured.

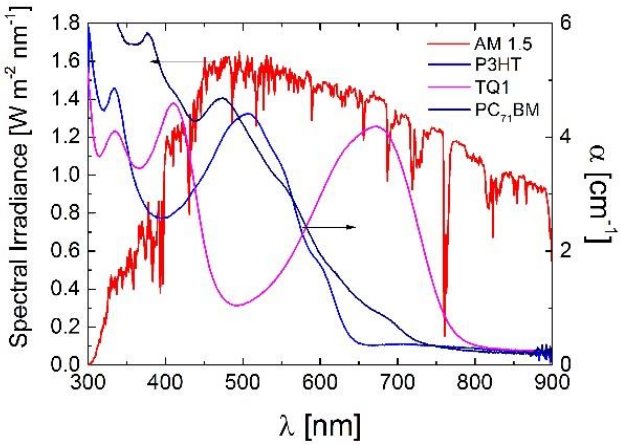

Figure 1.2. The AM 1.5 solar spectrum (red line) and the absorption spectrum of the conjugated polymers P3HT (blue), TQ1 (magenta) and $PC_{71}BM$ (dark blue).

The efficiency of a solar cell is determined by measuring the current voltage dependence under illumination. A typical current density-voltage ($J - V$) dependence of a solar cell under AM 1.5 illumination is shown in Figure 1.3. The power conversion efficiency (PCE or η) of a solar cell is given by:

$$PCE = \frac{J_{sc}V_{OC}FF}{P_{light}}, \tag{1.1}$$

where J_{sc} is the short circuit current density, V_{OC}, the open circuit voltage, FF the fill factor and P_{light} the power density of the illuminating light (for AM 1.5 P_{light}= 100 mW cm^{-2}). The fill factor is given by the ratio:

$$FF = \frac{J_{mp}V_{mp}}{J_{SC}V_{OC}}, \tag{1.2}$$

which describes the "squareness" of the $J - V$ curve; here J_{mp} and V_{mp} are the current density and voltage at the maximum power point, as shown in Figure 1.3.

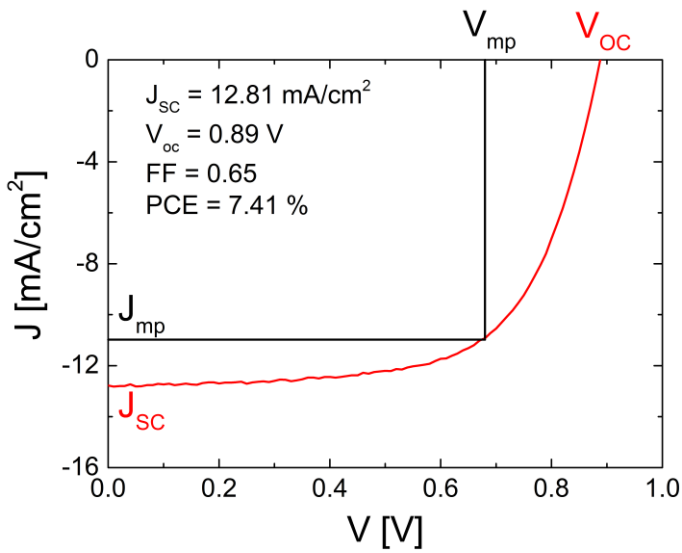

Figure 1.3. A current density-voltage plot (red line) of a solar cell under AM 1.5 illumination, showing the solar cell parameters, J_{SC}, V_{OC}, J_{mp} and V_{mp}.

1.3. Photogeneration of Charges

The generation of charges, i.e. free electrons and holes, as described previously, occurs through several steps in organic materials. This process is shown schematically in Figure 1.4a and an energy diagram of the photoexcitations is illustrated in Figure 1.4b. Upon photoexcitation, a bound electron-hole pair called a singlet exciton (S_1) is formed, where the spins of the electron and hole are antiparallel (↑↓). The singlet exciton has a short lifetime (~300 ps for P3HT) [25] and will decay ($k_{S1\rightarrow S0}$) to the ground state (S_0) unless a spin flip occurs transforming the singlet exciton into a triplet exciton ($k_{S1\rightarrow T1}$) or charge transfer takes place ($k_{S1\rightarrow CT}$). The spins of the electron and hole in a triplet exciton are parallel (↑↑) and the triplet typically has a long life time (ns-µs), as the decay to the ground state ($k_{T1\rightarrow S0}$) is forbidden by spin-selection rules [26]. The energy of the triplet state in organic materials has been found to lie 0.7-1.0 eV lower than the S_1 state [26–28].

Charge transfer (CT) states have been observed at the donor/acceptor interface in many organic BHJ blends [29–32]. The CT state is an excited state where the electron is located on the acceptor and the hole on the donor (as illustrated in Figure 1.4a), but is still Coulombically bound [29,30,33]. The CT state can be populated by charge transfer at the donor/acceptor interface

($k_{S1\rightarrow CT}$), or directly by excitation below the optical gap of the donor or acceptor (G_{CT}). Depopulation of the CT state can occur by decay to the ground state ($k_{CT\rightarrow S0}$) or to the triplet state ($k_{CT\rightarrow T1}$). The latter can be avoided if the energy of the triplet state (T_1) is located less than 0.1 eV below the CT state [29,34]. The CT state can dissociate into free charges (CS) if the Coulombically bound electron and hole can be separated ($k_{CT\rightarrow CS}$). Free charges can also recombine back into the CT state ($k_{CS\rightarrow CT}$) and then be lost by decaying to the ground state or to triplets. In addition to this, recombination of free charges to the ground state ($k_{CS\rightarrow S0}$) is also possible.

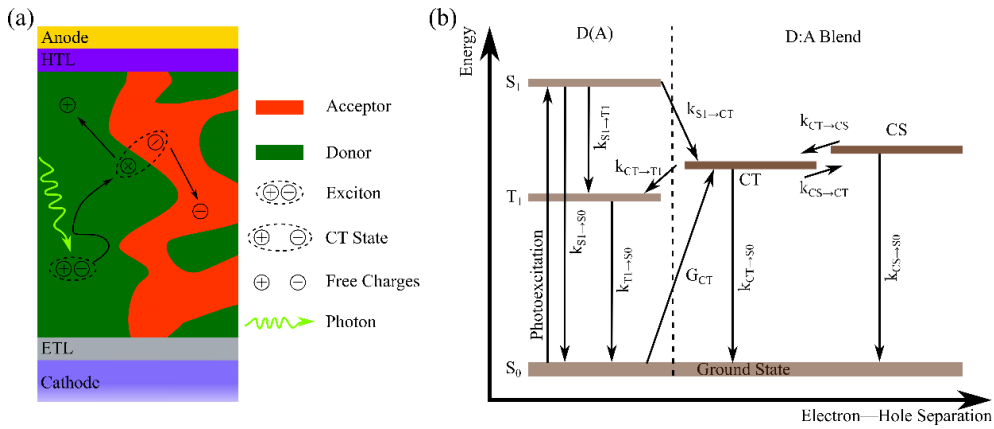

Figure 1.4 (a) A schematic illustration of the formation of an exciton upon absorption of a photon, the diffusion to a donor/acceptor interface and splitting into free electrons and holes which are transported to the cathode and anode, respectively. In (b) the energy schematic of the charge photogeneration process, including the possible types of photoexcitations and their decay processes are illustrated; for details see text.

The formation of electrons and holes in organic semiconductors is accompanied by a geometric deformation of the molecule itself. This leads to the formation of two states inside the bandgap, called a polaron, which is illustrated in Figure 1.5a and Figure 1.5b for a negative (P^-) and positive (P^+) polaron respectively. The polaron has two optically allowed transitions: P_1 and P_2 , which can be observed in photoinduced absorption measurements [35,36] **[Paper 3-5]**. In some organic materials which show ordered two-dimensional structures, delocalization of polarons has been

observed [35,37]. A positively charged delocalized polaron (DP^+) is shown schematically in Figure 1.5c along with the optically allowed transitions: DP_1 and DP_2, noting that DP_1 and DP_2 are red and blue shifted compared to P_1 and P_2, respectively [35]

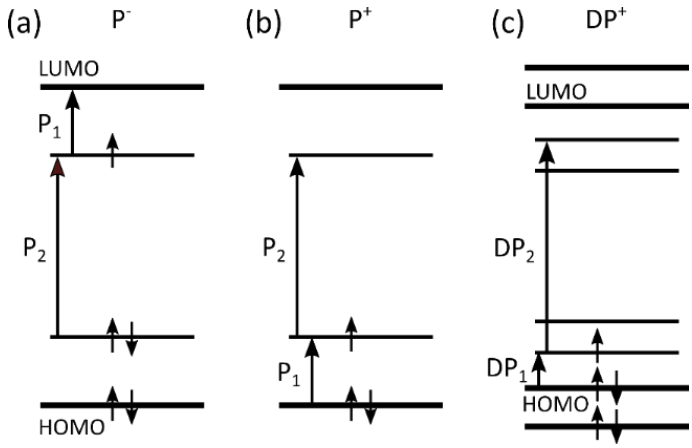

Figure 1.5. Schematic representation of the (a) P^- and (b) P^+ polaron, where the optically allowed transitions P_1 and P_2 are shown and in (c) the delocalized DP^+ polaron, showing the optically allowed DP_1 and DP_2 transitions.

1.4. Recombination

Recombination is the process where photoexcitations are lost and do not contribute to a current in semiconductors, making it a major loss process in solar cells. Several different recombination processes can occur in a solar cell, e.g. two free charge carriers recombining or a trapped and a free charge carrier recombining. Determining the dominating recombination type in organic solar cells and materials is an important part in designing new materials and devices.

Photoexcitations in organic materials can decay to the ground state through several different pathways. One can make a distinction between geminate and non-geminate recombination. Geminate recombination is when an electron and a hole created by the same photon recombines to the ground state; examples include exciton and CT recombination [30]. Non-geminate recombination is when holes and electrons from different photons recombine.

It is also useful to determine how the recombination rate (R) depends on the charge carrier concentration (n). In the case of monomolecular recombination, there is a linear dependence on the carrier concentration $R \propto n$, as shown in Figure 1.6a. Bimolecular recombination occurs when a free electron and hole meet and recombine (see Figure 1.6b). This recombination rate depends on the product of free holes and electrons: $R \propto np$, where n (p) is the concentration of electrons (holes). When charges are photogenerated, the number of generated holes and electrons is the same and the recombination rate has a quadratic dependence on the carrier concentration $R \propto np = n^2$, when $n = p$. In low-mobility materials, such as organic semiconductors, bimolecular recombination can be described using Langevin's theory [38] where the recombination rate is given by $R = \beta_L np$ and the bimolecular recombination constant is $\beta_L = \frac{e}{\varepsilon_r \varepsilon_0}(\mu_n + \mu_p)$, where e is the elementary charge, ε_r (ε_0) the relative (vacuum) permittivity and μ_n (μ_p) the electron (hole) mobility. It should be noted that the experimentally obtained recombination constant in several BHJ blends has been observed to be reduced compared to that expected from Langevin recombination [39–41]. This reduced bimolecular recombination is typically represented by including a reduction factor in the recombination rate: $R = \zeta \beta_L np$, where $\zeta = \beta / \beta_L$.

A special case of Langevin recombination can occur when the transport of charge carriers is restricted to two dimensions (2D), which has been observed for materials which show a high degree of ordering. The recombination rate will have the following dependence on the charge carrier density: $R \propto (np)^{5/4}$, which in the case of $n = p$ becomes $R \propto n^{5/2}$ [42–44] **[Paper 3]**.

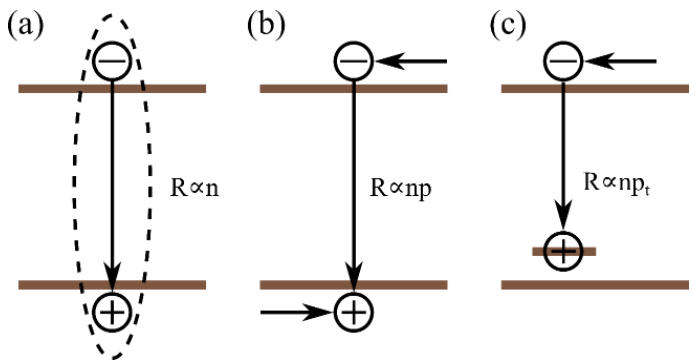

Figure 1.6. Schematic representation of (a) monomolecular, (b) bimolecular and (c) trap-assisted recombination.

Trap-assisted recombination occurs when one charge carrier is in a trap which recombines with a free charge carrier, the situation where a trapped hole recombines with a free electron is shown in Figure 1.6c. Here, the recombination rate depends on the concentrations of charge carriers in traps and free carriers: $R \propto np_t$. The traps in a material can be distributed in several different ways. For single level traps, as shown in Figure 1.6c, all traps are located at the same energy. Another type of distribution is the exponential trap-distribution which is shown in Figure 1.7. Here there is an exponential distribution of electron traps below the LUMO level and hole traps above the HOMO level. The width of the transport states in the HOMO (LUMO) level is given by W [45] **[Paper 3-5]**. In materials having an exponential distribution of traps, the recombination rate will depend on the charge density as: $R \propto n^{\delta}$, where the effective reaction order: $\delta > 2$ and is temperature dependent [46–49] **[Paper 3]**.

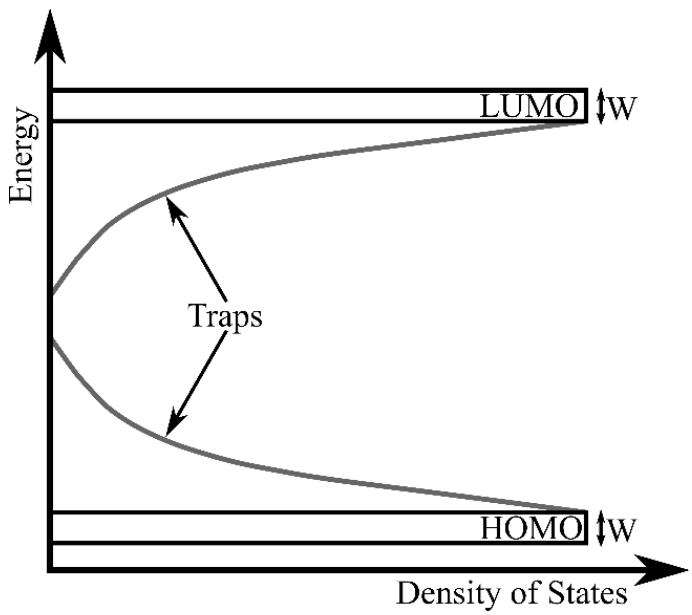

Figure 1.7. Schematic of an exponential distribution of electron (hole) traps below (above) the LUMO (HOMO) levels having transport states with the width W.

The above discussion concerns recombination that typically occurs in the bulk of the material. Surface recombination can be seen if the injection and/or extraction of charges at the contacts is limited [50–52]. When surface

recombination dominates, S-shaped $J - V$ curves have been observed and can reduce the V_{OC} [51–53].

1.5. Contacts in Organic Solar Cells

Contacts are an essential part of all optoelectronic devices, the purpose of which is to ensure efficient injection/extraction of charge carriers. Ideally the anode and cathode should form ohmic contacts to the donor and acceptor, respectively. In addition to this, the extraction of electrons (holes) at the anode (cathode) should be prevented. The energy diagram of a solar cell is shown in Figure 1.8a in a flat-band condition. Here, the anode and cathode have work functions (Φ_{an} and Φ_{cat}) matching the HOMO of the donor and the LUMO of the acceptor, respectively. When the solar cell is short circuited the Fermi-level inside the device aligns, as illustrated in Figure 1.8b. A built-in voltage (U_{bi}) is formed by the difference in the work function of the anode and cathode and will drive electrons (holes) to the cathode (anode).

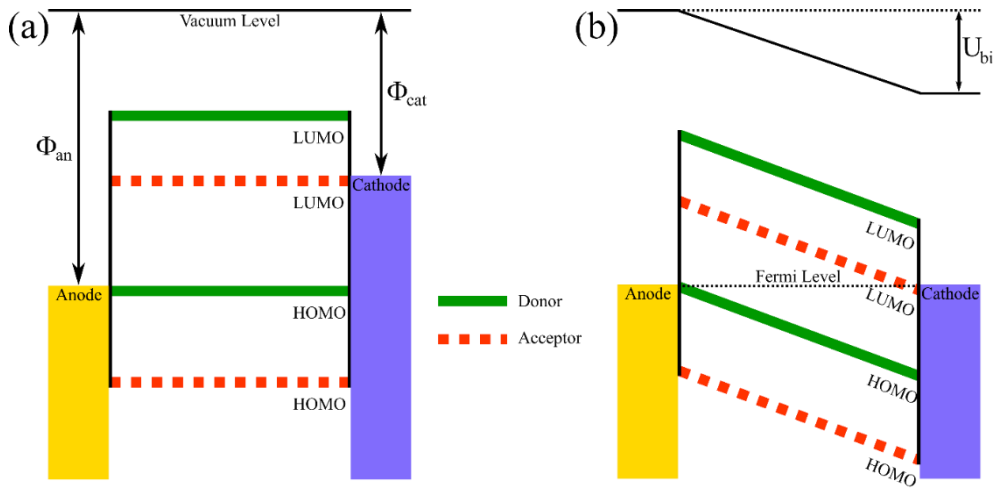

Figure 1.8. Energy diagram of a BHJ solar cell (a) in flat-band and (b) at short-circuit

If the Fermi-level at the contact is close to the HOMO or the LUMO level of the organic semiconductor, vacuum level shifts at the contact/organic interface are frequently observed [54,55]. This vacuum level shift has been suggested to be caused by the formation of an interfacial dipole at the

organic/contact interface. The integer charge transfer (ICT) model [55–57] explains the dipole formation by suggesting that interfacial states exist within the bandgap of the organic semiconductor. The positive (negative) integer charge transfer E_{ICT+} (E_{ICT-}) state is defined as the energy required (gained) to remove (by adding) one electron from (to) the organic semiconductor at the interface. These ICT states have been observed experimentally [55,58–60]. The energy level alignment will depend on the energy of the ICT states and the work function of the contact. The situation where the work function of the contact is higher than E_{ICT+} is shown in Figure 1.9a. After contact between the two materials is made, electrons are transferred from the organic semiconductor to the contact until the Fermi-level is pinned at E_{ICT+}, forming an interfacial dipole (Δ) at the interface. When the work function lies lower in energy than E_{ICT-}, as shown in Figure 1.9b, electrons will flow from the contact into the organic semiconductor until E_{ICT-} is pinned at the Fermi-level, forming an interfacial dipole. If the work function lies between E_{ICT-} and E_{ICT+}, no electron transfer occurs.

Interfacial dipole formation has also been suggested to occur at organic/organic interfaces [59,60]. In a donor:acceptor blend, where the donor E_{ICT+} lies lower in energy than the acceptor E_{ICT-}, electron transfer will occur from the donor to the acceptor until energy alignment occurs, forming an interfacial dipole, as shown in Figure 1.9c. As a consequence, Bao et al. suggested that an interfacial dipole limits the maximum obtainable V_{OC} and that an interfacial dipole can act as a recombination center, leading to increased trap-assisted recombination [60].

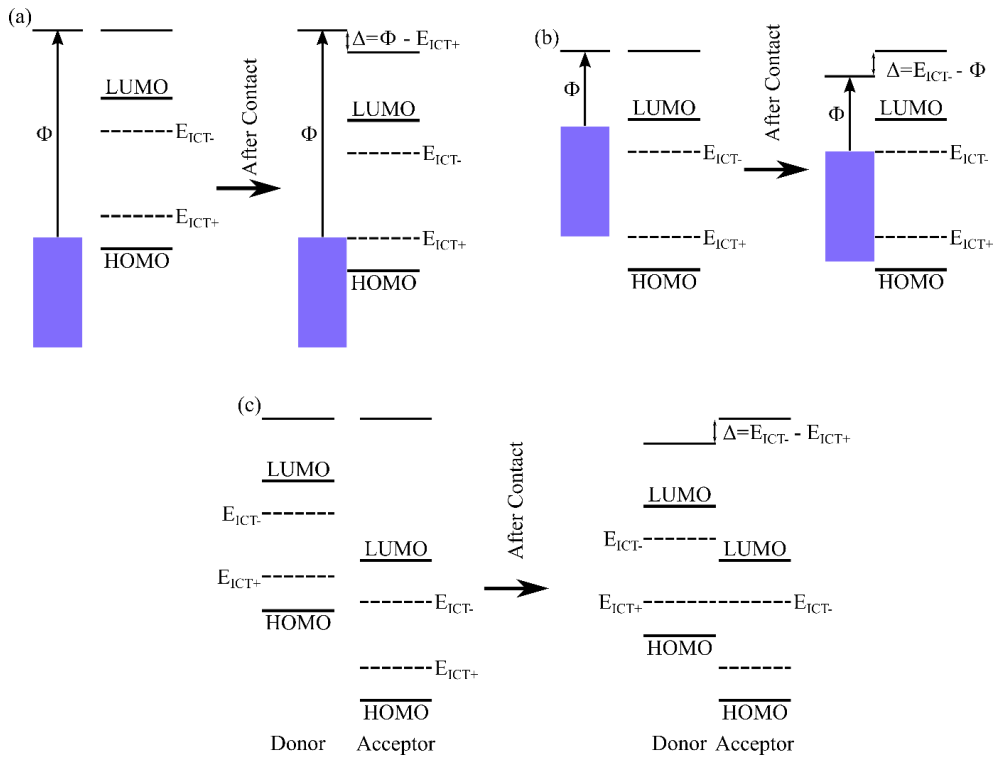

Figure 1.9. Schematic illustration of the ICT model, before and after contact between the different materials occurs, showing (a) when $\Phi > E_{ICT+}$, (b) $\Phi < E_{ICT-}$ and (c) between a donor and acceptor where $E_{ICT+} < E_{ICT-}$.

1.6. Aim of the Thesis

In this work, two different characterization techniques have been utilized to clarify the charge transport and recombination behavior of injected and photogenerated charge carriers in a variety of organic bulk-heterojunction blends and devices. In **[Paper 1 & 2]**, the CELIV and photo-CELIV techniques have been used to characterize the effect a hole blocking layer has on the charge transport and recombination in devices having a P3HT:PC_{60}BM blend.

The determination of the dominating bulk recombination type in BHJ blends is of importance to enable the development of efficient organic solar cells. The photoinduced absorption (PIA) technique is used in **[Paper 3]**, where it is shown how to use PIA to obtain the dominating recombination type in the model system pBTTT:PC_{60}BM. This blend was chosen due to the

fact that the dominating recombination process can be varied between trap-assisted and 2D Langevin recombination by controlling the blend ration. In 1:1 blends trap-assisted recombination is observed while 1:4 blends exhibit 2D Langevin recombination [44].

To determine the effect an interfacial dipole has on the recombination of photogenerated charge carriers, the PIA technique was applied to three different BHJ blends. In **[Paper 4]**, P3HT:$PC_{60}BM$ and P3HT:ICBA were characterized, as the former is expected to have a large interfacial dipole at the polymer/fullerene interface while the latter shows no sign of a dipole [60]. Both blends exhibit ordering of the polymer (P3HT) leading to reduced bimolecular recombination. Finally, the recombination of the amorphous polymer TQ1 in blends with the fullerene derivative $PC_{71}BM$ was clarified using the PIA technique. These blends have been suggested to have no interfacial dipole **[Paper 5]**.

2. Charge Extraction by Linearly Increasing Voltage

Charge extraction by linearly increasing voltage (CELIV) is a transient measurement technique which has been used to clarify the charge transport and recombination behavior in both inorganic [61–63] and organic [63–70] low-mobility materials and devices. In CELIV, a linearly increasing voltage pulse is typically applied to a sandwich type device. The mobility, μ, and the charge concentration, n, can be simultaneously obtained from a CELIV measurement. The technique can be divided into several different operating modes: dark-CELIV (or simply CELIV) when measuring equilibrium charge carriers in the dark [61,64]; photo-CELIV when charges are photogenerated [62,65,66]; and metal-insulator-semiconductor-CELIV (MIS-CELIV) or injected-CELIV (i-CELIV) [71–77], when one of the contacts is an insulator. In the last case, an offset voltage is used to inject one type of carrier which accumulates at the insulator/semiconductor interface and then extracted by the CELIV pulse. In addition to these modes, the technique can also be used to determine the doping concentration using doping-CELIV [78].

The linearly increasing voltage pulse having the rise speed: $A = V_{appl}/t_{pulse}$, and the current response is shown in Figure 2.1a and 2.1b, respectively. The current response consists of two parts: the displacement, $j(0)$, and extraction, Δj, currents. The displacement current is caused by the geometric capacitance, C, of the device given as:

$$C = \frac{j(0)S}{A}, \tag{2.1}$$

where S is the contact area. From the displacement current, the thickness, d, of the device can be determined:

$$d = \frac{A\varepsilon_r\varepsilon_0}{j(0)}, \tag{2.2}$$

where ε_r is the dielectric constant (relative permittivity) of the active material and ε_0 the vacuum permittivity. The number of charges which are extracted by the voltage pulse can be obtained by integrating the extraction current:

$$n = \frac{2}{ed}\int_0^{t_{pulse}} \Delta j dt, \tag{2.3}$$

where e is the elementary charge.

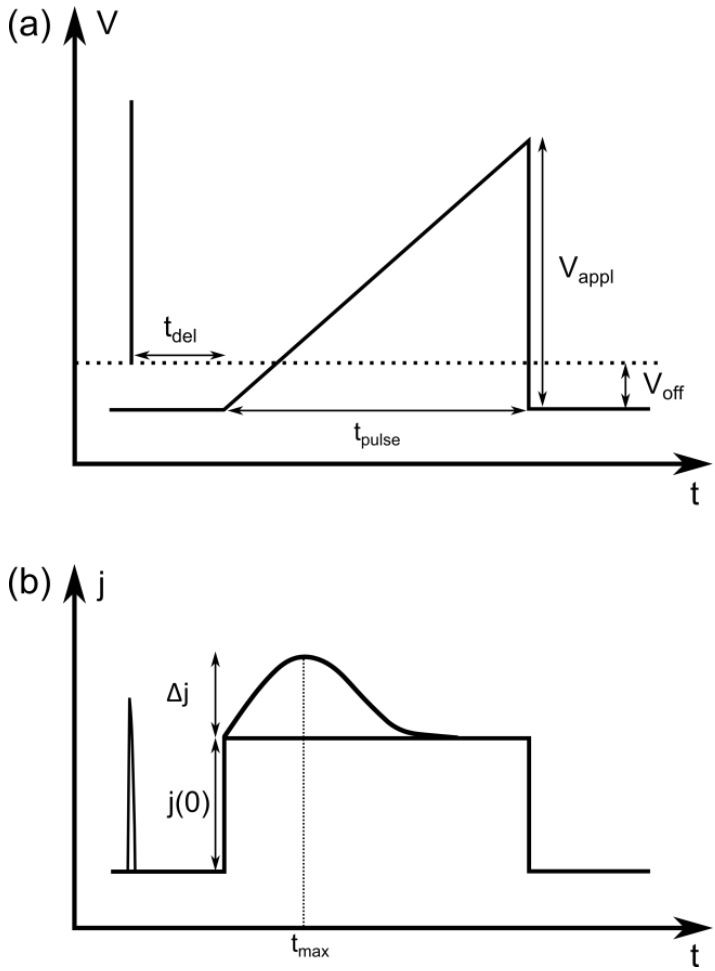

Figure 2.1 Schematic illustration of the CELIV technique, showing (a) the applied voltage pulse and (b) the resulting current transient.

The mobility can be determined from a CELIV measurement by determining t_{max}, which is the time when the extraction current reaches its maximum value as illustrated in Figure 2.1b. The mobility can then be calculated using:

$$\mu = K \frac{d^2}{A t_{max}^2 \left(1 + 0.36 \frac{\Delta j}{j(0)}\right)}, \tag{2.4}$$

where the constant K is 2/3 in the case of volume generation and 2 for surface generation. The factor $(1 + 0.36)$ is a numerically estimated correction factor [61,64]. Note that other correction factors have been suggested by other

authors [79–81]. Juška et al. also showed that for photogenerated charge carriers, the absorption profile needs to be taken into account to avoid large errors in the mobility estimation [82]. In addition to this, if doping is present in the active material Sandberg et al. [78] showed that the depletion width caused by the dopants needs to be taken into account to avoid overestimating the mobility.

In photo-CELIV, a laser pulse is typically used to generate charge carriers and the voltage pulse is applied after a delay time, t_{del}, as illustrated in Figure 2.1. By varying the delay time, the lifetime of the charge carriers, the recombination type and the recombination constant (for bimolecular recombination) can be obtained [42,44,63,66–69,83].

2.1. MIS-CELIV

One of the disadvantages with the CELIV and photo-CELIV technique is that the type of charge carrier cannot be distinguished in the measurement. To be able to determine the hole and electron mobility separately, Juška et al. developed the metal-insulator-semiconductor CELIV (MIS-CELIV) technique [71], also called i-CELIV [72,74,76]. In MIS-CELIV, an insulator is inserted between one of the contacts and the semiconductor. By applying a negative (positive) offset voltage on the insulator, holes (electrons) can be accumulated at the insulator/semiconductor interface and subsequently extracted by a CELIV pulse, as schematically illustrated in Figure 2.2.

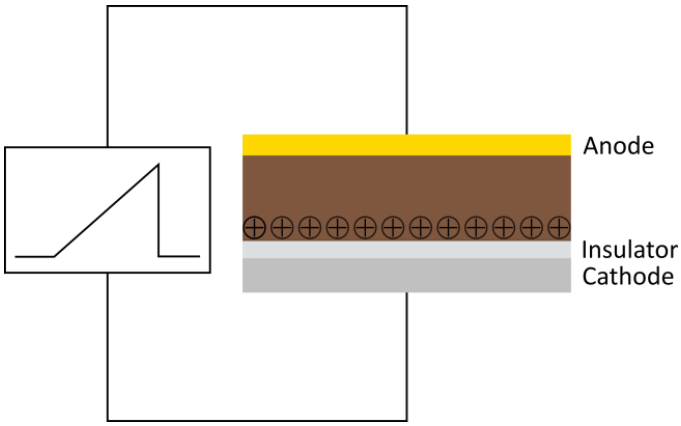

Figure 2.2 Schematic of the MIS-CELIV technique, where an applied negative offset injects holes, which are accumulated at the insulator/semiconductor interface and the CELIV pulse extracts the accumulated carriers.

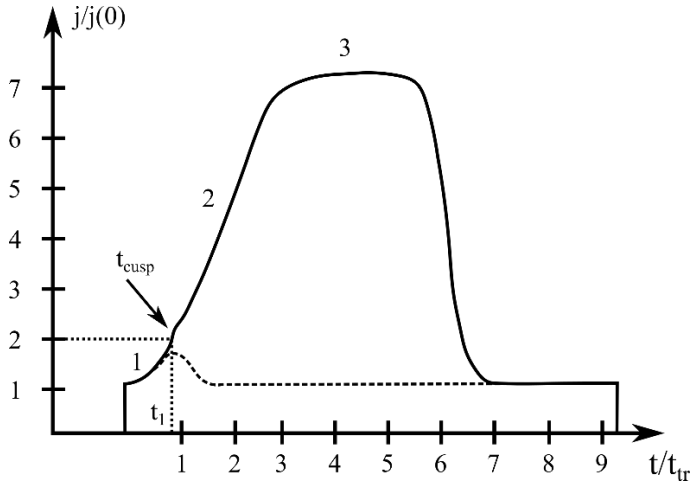

Figure 2.3 Schematic of the shape of the MIS-CELIV transient, for explanation of the different parameters see text.

A schematic MIS-CELIV current transient is shown in Figure 2.3. In contrast to CELIV, the MIS-CELIV transient ideally consists of three different regimes [71,75]. It should be noted that in the initial MIS-CELIV work by Juška et al. the insulator capacitance was assumed to be much larger than the semiconductor capacitance [71]. Sandberg et al. derived expressions int the case of a finite insulator capacitance [75], which will be used here. Initially when $t < t_{cusp}$ (region 1 in Figure 2.3) with $t_{cusp} = 0.92t_{tr}$, the current will follow [75]:

$$j(t) = j_0\left[1 + \tan^2\left(\frac{t}{t_{tr}}\sqrt{\frac{1}{1+f}}\right)\right]. \tag{2.5}$$

The transit time for charge carriers is given by:

$$t_{tr} = \sqrt{\frac{2d_s^2}{\mu A}(1+f)}, \tag{2.6}$$

where $f = \frac{\varepsilon_s d_I}{\varepsilon_I d_s}$ is the ratio between the capacitance of the semiconductor and insulator layers; ε_s (ε_I) is the relative permittivity of the active layer (insulator) and d_s (d_I) is the thickness of the active layer (insulator).

When $t > t_{cusp}$ (region 2) the current will grow as:

$$j(t) = j_0 + (j_{sat} - j_0)\tanh^2\left(\frac{3t}{2t_{tr}}\sqrt{\frac{j_0}{j_{sat}}}\right), \tag{2.7}$$

where j_{sat} is saturation current (region 3) given by:

$$j_{sat} = \frac{\varepsilon_I \varepsilon_0 A}{d_i}. \tag{2.8}$$

If a small offset is applied such that a small extraction current is obtained, $\Delta j \leq j(0)$ (dashed line in Figure 2.3) the mobility can be obtained using Equation (2.6). However, if a large reservoir is formed at the insulator/semiconductor interface, then space charge limited current (SCLC) extraction is obtained. In this case, a super-linear increase of the extraction current is obtained and the mobility can be determined from kink near t_{cusp} as shown in Figure 2.3. However, this kink is typically difficult to discern in a measurement [71,73,75,76]. To enable estimation of the mobility in the case of SCLC extraction one can use the time when the extraction current $\Delta j = j(0)$, as illustrated by the dotted line in Figure 2.3, given by t_1 which is related to the transit time by:

$$t_1 = \frac{\pi}{4} t_{tr}. \tag{2.9}$$

Using Equations (2.9) and (2.6) the mobility in the case of SCLC extraction is obtained by:

$$\mu = \frac{\pi^2 d_s^2}{8At_1^2}(1+f)^2. \tag{2.10}$$

When a MIS-CELIV measurement is performed, an ohmic injecting contact is typically used to ensure efficient injection of charge carriers into the device. However, in this case diffusion of charges into the device needs to be accounted for, to avoid making errors in estimating the mobility as shown by Sandberg et al. [75]. To minimize the error in the estimation of the mobility a correction factor accounting for the diffusion was made, resulting in the following equation:

$$\mu = \frac{\pi^2 d_s^2}{8At_1^2}(1+f)^2\left[1 + \frac{\pi^4 kT(1+f)}{2eAt_1}\right]^{-1}. \tag{2.11}$$

2.2. Simulating CELIV Transients

To gain further insight into the charge transport and recombination behavior in organic devices, simulating the behavior using a 1-D drift-diffusion model has been shown to be of use [50,51,53,78,84] **[Paper 1 & 2]**. The model describes the BHJ layer an effective semiconductor where the LUMO level is that given by the acceptor and the HOMO level by the donor, as illustrated in Figure 2.4.

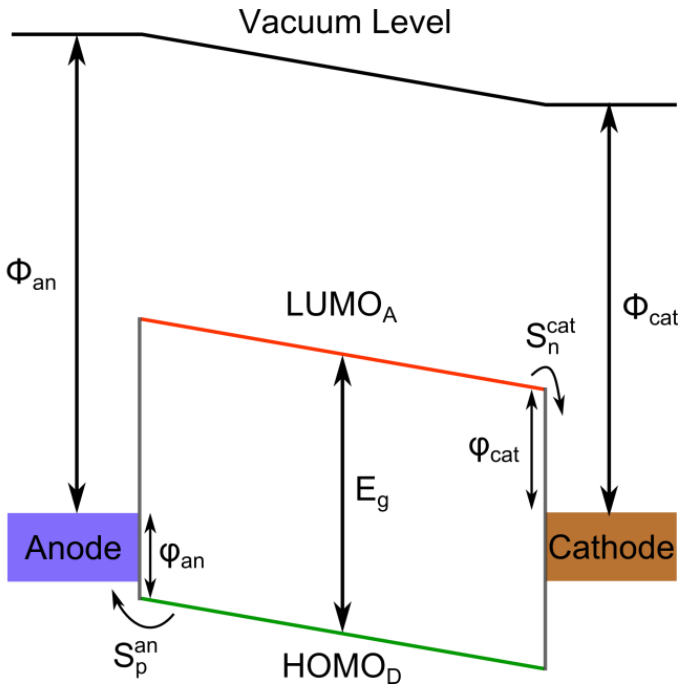

Figure 2.4 A schematic drawing of the device structure used in the drift-diffusion model, see text for the description of the parameters.

In the model, the continuity and the Poisson equations are numerically solved [**Paper 1 & 2**] [50,51,78]. The description of the extraction and injection of charge carriers at the contacts has been made using the surface recombination velocity, $S_{n,p}^{an,cat}$. This property describes the rate at which charges are extracted at the semiconductor/contact interface. In the case of a

perfectly extracting anode the surface recombination rate is $S_p^{an} = \infty$, for majority carriers, and a perfectly blocking anode has $S_n^{an} = 0$, for minority carriers [50]. The current densities at the anode are given by [**Paper 1 & 2**] [50,53,85,86]:

$$J_p(0) = -eS_p^{an}\left(p(0) - N_{HOMO}e^{-\frac{\varphi_{an}}{kT}}\right), \tag{2.12}$$

$$J_n(0) = -eS_n^{an}\left(n(0) - N_{LUMO}e^{-\frac{E_g-\varphi_{an}}{kT}}\right), \tag{2.13}$$

where φ_{an} is the injection barrier for holes at the anode (φ_{cat} is similarly the injection barrier for electrons at the cathode). The currents at the cathode can be described in an analogous way **[Paper 2]**.

3. Photoinduced Absorption

Photoinduced absorption is a technique where a pump beam generates photoexcitations and a probe is used to detect these excitations. In a measurement, the change in absorption caused by the generated photoexcitations is typically made by monitoring the change in transmission, ΔT, which is normalized to the transmission, T, in the ground state. The relative change in transmission can be related to the change in absorption, $\Delta\alpha$, and the amount of photoexcitations, N, through:

$$-\frac{\Delta T}{T} = d\Delta\alpha = N\sigma d, \tag{3.1}$$

where d is the thickness of the sample and σ is the absorption cross section, assumed to be 10^{-16} cm^2 [87]. The latter part of Equation (3.1) holds for a thin film, where $\alpha_L d \ll 1$, and α_L is the absorption coefficient at the pump wavelength. For a thick film, i.e. $\alpha_L d \gg 1$, the sample thickness can be replaced by the effective optical thickness: $d_{eff} = 1/\alpha_L$ [88].

3.1. Continuous wave photoinduced absorption

In a continuous wave photoinduced absorption (PIA) measurement, the pump beam is modulated at a specific frequency and the change in transmission is detected by a phase sensitive lock-in amplifier. In this case, the relative change in transmission is given as two components: in-phase and quadrature. The in-phase (PA_I) component has a 0° phase shift and the quadrature (PA_Q) has a 90° phase shift compared to the pump beam. The photoinduced absorption, as a function of the angular frequency $\omega = 2\pi f$, where f is the frequency, can be represented in complex form as:

$$-\frac{\Delta T}{T} = PA(\omega) = PA_I(\omega) - iPA_Q(\omega). \tag{3.2}$$

The photoinduced absorption can also be represented in polar coordinates as [36,88]:

$$PA(\omega) = PA_R e^{-i\varphi(\omega)}, \tag{3.3}$$

where PA_R is the radius signal and $\varphi(\omega)$ the phase. The radius signal is related to the in-phase and quadrature signals as:

$$PA_R = \sqrt{PA_I^2 + PA_Q^2}, \tag{3.4}$$

and the phase is given by:

$$\varphi(\omega) = \arctan\left(\frac{PA_Q}{PA_I}\right). \tag{3.5}$$

The lifetime can also be obtained from the phase as:

$$\varphi = \arctan(\omega\tau), \tag{3.6}$$

and now the lifetime is given by:

$$\tau = \omega^{-1}\arctan(\varphi). \tag{3.7}$$

Thus, by obtaining the in-phase and quadrature signals, the lifetime of the photoexcitations can be determined directly from these components.

To describe the dynamics of photoexcitations in a PIA experiment one typically solves a rate equation having monomolecular and/or bimolecular recombination with a periodic generation. Westerling et al. solved a rate equation which included mono- and bimolecular recombination:

$$\frac{dN(t)}{dt} = G(t) - \frac{N(t)}{\tau} - \beta N(t)^2, \tag{3.8}$$

where $G(t) = \frac{G}{2}(1+\cos(\omega\tau))$ is the generation, τ the monomolecular lifetime and β the bimolecular recombination constant. The following analytical expressions for the in-phase and quadrature components were obtained [89]:

$$PA_I = \left(\frac{G\tau}{2}\right)\left(\frac{\omega_1\tau}{(\omega_1\tau)^2+(\omega\tau)^2}\right)\sigma d, \tag{3.9}$$

$$PA_Q = \left(\frac{G\tau}{2}\right)\left(\frac{\omega\tau}{(\omega_1\tau)^2+(\omega\tau)^2}\right)\sigma d, \tag{3.10}$$

$$\omega_1\tau = \sqrt{-\frac{1}{2}\left((\omega\tau)^2-2\left(\tau/\tau_\beta\right)^2-1\right)+\frac{1}{2}\sqrt{\left((\omega\tau)^2+2\left(\tau/\tau_\beta\right)^2+1\right)^2-2\left(\tau/\tau_\beta\right)^4}}, \tag{3.11}$$

where the bimolecular lifetime is given by $\tau_\beta = 1/\sqrt{G\beta}$. If the photoexcitations are dominated by bimolecular recombination, the monomolecular lifetime $\tau \to \infty$ and Equations (3.9)-(3.11) become:

$$PA_I = \left(\frac{G\tau_\beta}{2}\right)\left(\frac{\omega_0\tau_\beta}{(\omega_0\tau)^2+(\omega\tau_\beta)^2}\right)\sigma d, \tag{3.12}$$

$$PA_Q = \left(\frac{G\tau_\beta}{2}\right)\left(\frac{\omega\tau_\beta}{(\omega_0\tau_\beta)^2+(\omega\tau_\beta)^2}\right)\sigma d, \tag{3.13}$$

$$\omega_0\tau_\beta = \sqrt{-\frac{1}{2}\left((\omega\tau_\beta)^2-2\right)+\frac{1}{2}\sqrt{\left((\omega\tau_\beta)^2+2\right)^2-2}}, \tag{3.14}$$

The analytical solution of Equation (3.13) has been shown to give an incorrect intensity dependence for the quadrature component at near steady state conditions ($\omega\tau_\beta \ll 1$) [90,91]. By solving Equation (3.8), assuming that bimolecular recombination dominates i.e. $\tau \to \infty$, Westerling et al. showed that the quadrature has the following expression at high intensities [91]:

$$-PA_Q = \frac{\omega\sigma d}{2\pi\beta}\ln\left(\frac{C_1\beta G\exp(-\alpha_L d/2)}{\omega^2}\right), \tag{3.15}$$

where $C_1 = 1.46111$. Thus, by plotting the intensity dependence of the quadrature component on a lin-log scale the slope will be given by $(\omega\sigma d/2\pi\beta)$ from which the bimolecular recombination constant can be directly determined.

The dispersive nature of charge transport in organic materials leads to dispersive recombination dynamics. To describe this behavior using frequency dependent generation Epshtein et al. used a Cole-Cole type expression, given in complex form as [92,93]:

$$PA_I(\omega) - iPA_Q(\omega) = G\tau_0\frac{\sigma d}{1+(i\omega\tau_0)^\gamma}, \tag{3.16}$$

where the dispersion parameter γ takes values: $0 < \gamma < 1$, where $\gamma = 1$ corresponds to a non-dispersive behavior and τ_0 is an effective lifetime. The effective lifetime will be independent of the pump intensity if the recombination process is monomolecular, i.e. $\tau_0 = \tau$, and depend on the excitation intensity if it is bimolecular: $\tau_0 = 1/\sqrt{\bar{\beta}G}$, where $\bar{\beta}$ is a mean bimolecular recombination constant [36,88,91,93]. The in-phase and quadrature components are now given by [88,94]:

$$PA_I = \frac{G\tau_0\left[1+\cos\left(\frac{\pi}{2}\gamma\right)(\omega\tau_0)^\gamma\right]\sigma d}{1+2\cos\left(\frac{\pi}{2}\gamma\right)(\omega\tau_0)^\gamma+(\omega\tau_0)^{2\gamma}}, \tag{3.17}$$

$$PA_Q = \frac{G\tau_0\sin\left(\frac{\pi}{2}\gamma\right)(\omega\tau_0)^\gamma\sigma d}{1+2\cos\left(\frac{\pi}{2}\gamma\right)(\omega\tau_0)^\gamma+(\omega\tau_0)^{2\gamma}}. \tag{3.18}$$

The phase can also be expressed in the dispersive regime as:

$$\varphi = \arctan\left(\frac{\sin\left(\frac{\pi}{2}\gamma\right)(\omega\tau)^\gamma}{1+\cos\left(\frac{\pi}{2}\gamma\right)(\omega\tau)^\gamma}\right), \tag{3.19}$$

and the lifetime is now obtained as

$$\tau = \omega^{-1}\left(\frac{\sin(\varphi)}{\sin\left(\frac{\pi}{2\gamma}-\varphi\right)}\right)^{1/\gamma}. \tag{3.20}$$

3.2. Modeling Photoinduced Absorption

One disadvantage with the PIA technique is that measurements are made in frequency space. Analytical solutions of the rate equation can be obtained in the case of a sinusoidal generation [89]. However, obtaining analytical expressions in the case of square wave generation, typically achieved in experiments with a mechanical chopper, is difficult if not impossible. However, numerical simulations can always be utilized. For an arbitrary reaction order, δ, given by the following rate equation **[Paper 3]**:

$$\frac{dN(t)}{dt} = G(t) - bN(t)^\delta, \tag{3.21}$$

where $N(t)$ is the charge carrier density, $G(t)$ the photogeneration, which in this case is a square wave with the height G and angular frequency ω and b is an arbitrary recombination constant. To obtain the PIA behavior after solving Equation (3.21), the in-phase and quadrature components are obtained from [91]:

$$PA_I = \frac{\omega\sigma d}{\pi}\int_c^{c+2\pi/\omega} N(t)\sin(\omega t)dt, \tag{3.22}$$

$$PA_Q = -\frac{\omega\sigma d}{\pi}\int_c^{c+2\pi/\omega} N(t)\cos(\omega t)dt, \tag{3.23}$$

where c is an arbitrary point in time. Assuming near steady state conditions ($\omega\tau \ll 1$), Wilson et al. [48,49] showed that the in-phase will depend on the generation as:

$$PA_I \propto G^{1/\delta}, \tag{3.24}$$

thus, the reaction order can be obtained from the intensity dependence. The reaction order can also be determined from the quadrature signal which at near steady state follows [48,49]:

$$PA_Q \propto \omega^{1/(\delta-1)}. \tag{3.25}$$

It should be noted that when $\delta \approx 2$, the quadrature will be given by Equation (3.15).

The description of trap-assisted recombination can be made by adding a term which accounts for traps, leading to the following rate equation:

$$\frac{dN(t)}{dt} = G(t) - \beta n(t)^2 - Cn(t)n_t(t), \tag{3.26}$$

where, $N = n + p + n_t + p_t$ is the total density of charge carriers and n (p) is the density of free electrons (holes) and n_t (p_t) the density of trapped electrons (holes) and C is the capture coefficient. Note that symmetry between electrons and holes has been assumed in Equation (3.26), i.e. $n = p$ and $n_t = p_t$.

To describe the dynamics, a multiple trapping and retrapping model is used [45]. A continuous distribution of states is assumed for free charges (ρ_C) and an exponential distribution for trapped charges (ρ_t), giving the following expressions for electrons:

$$\rho_C(E) = \frac{N_C}{W}, \tag{3.27}$$

$$\rho_t(E) = \frac{N_t}{E_{ch}} \exp\left(\frac{E-E_C}{E_{ch}}\right), \tag{3.28}$$

where N_C is the to density of states in the conduction band (LUMO level) and W is its width (this is illustrated in Figure 1.7). The trap distribution has the total density of trap states N_t, the mean trap depth is described by the characteristic energy E_{ch} and the bottom of the conduction band is E_C. The density of free electrons is obtained, assuming that the Fermi-level is far from the conduction band edge, as:

$$n = \int_{E_C}^{E_C+W} \rho_C(E)F(E)dE \approx N_C^* \exp\left(\frac{E_F - E_C}{kT}\right), \tag{3.29}$$

$$N_C^* = N_C \frac{kT}{W}\left(1 - \exp\left(-\frac{W}{kT}\right)\right). \tag{3.30}$$

In this model, the trap depth is assumed to be $E_{ch} > kT$ and the trapped charges are assumed to follow a Fermi-Dirac distribution, giving the density of trapped charges:

$$n_t \approx \int_{-\infty}^{E_F} \rho_t(E)dE = N_t \exp\left(\frac{E_F - E_C}{E_{ch}}\right). \tag{3.31}$$

A relation between the trapped and free charges can be obtained by combining Equation (3.29) with (3.31):

$$n_t = N_t \left(\frac{n}{N_C^*}\right)^{kT/E_{ch}}. \tag{3.32}$$

By assuming that the concentration of traps is much larger than the number of free carriers, the recombination will depend on $R \propto nn_t$ and by using Equation (3.32), $R \propto n_t^{1+E_{ch}/kT}$ is obtained. Therefore, an effective reaction order for traps is given by:

$$\delta(T) = 1 + \frac{E_{ch}}{kT}. \tag{3.33}$$

Note that in this case δ is temperature dependent. It is possible to distinguish between trap-assisted and free carrier recombination by determining the possible temperature dependence of the reaction order from Equations (3.24) and (3.25).

4. Experimental

4.1. Materials

In this work, three different donor materials and three different acceptors were used. The donors were conjugated polymers and the acceptors fullerene derivatives. The conjugated polymers used were poly(3-hexylthiophene) (P3HT), poly[2,5-bis(3-tetradecylthiophen-2-yl)thieno[3,2-b]thiophene] (pBTTT) and poly[2,3-bis-(3-octyloxyphenyl)quinoxaline-5,8-diyl-alt-thiophene-2,5-diyl] (TQ1). As acceptor materials, the fullerene derivatives [6,6]-phenyl C61 butyric acid methyl ester ($PC_{60}BM$), [6,6]-phenyl-C_{71}-butyric acid methyl ester ($PC_{71}BM$) and indene-C_{60} bisadduct (ICBA) were used. The chemical structures of the materials are shown in Figure 4.1. All processing of the organic semiconductors were made in a nitrogen filled glovebox.

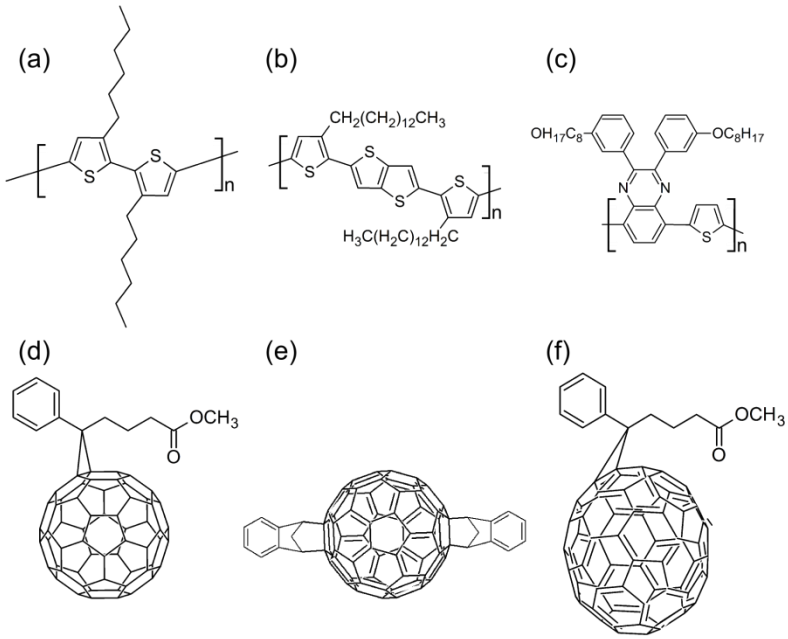

Figure 4.1 The chemical structures of the organic semiconductors (a) P3HT, (b) pBTTT, (c) TQ1 (d) $PC_{60}BM$, (e) ICBA and (f) $PC_{71}BM$

The devices in the CELIV measurements **[Paper 1 & 2]** used a P3HT:$PC_{60}BM$ 1:1 blend. This blend was spin coated onto indium tin oxide (ITO) substrates with or without a pre-coated TiO_2 layer, resulting in thicknesses between 600 and 900 nm. After the spin coating, a 30 nm copper electrode was evaporated on top to complete the devices. Following the deposition of the top contact, the devices were heat treated at 120°C for 15 minutes inside the glovebox.

The TiO_2 layers were prepared by dip coating the substrates in a titanium chloride ($TiCl_4$) solution. The $TiCl_4$ was dissolved in a solvent mixture of ethanol (EtOH) water (H_2O) and tetrahydrofuran (THF) along with the surfactant Pluronic 127. The final mixture had the molar ratio 1:250:10:20:0.001 ($TiCl_4$:EtOH:H_20:THF:Pluronic 127). The ITO substrates were immersed into the $TiCl_4$ solution and withdrawn at a constant speed of 1.2 mm s^{-1} at room temperature and at a constant humidity of 25%. To form the anatase TiO_2 crystal structure, the dried films were heated at 500° C for 10 minutes. To obtain thicker films, the substrates were dipped several times, with a heat treatment of 400° C for 3 minutes between each dipping step and finally sintered at 500° C. The crystallinity and the thickness of the films were determined using x-ray diffraction and x-ray reflection measurements, respectively, using the Bruker D8 Discover instrument **[Paper 1 & 2]**.

For the PIA measurements on pBTTT:$PC_{60}BM$ 1:1 and 1:4 blends **[Paper 3]** the semiconductors were dissolved in 1,2-dicholobenzene. The blend mixtures and the cleaned sapphire substrates were heated to 80° C prior to spin coating. The P3HT:$PC_{60}BM$ and P3HT:ICBA blends **[Paper 4]** were made from solutions made using chlorobenzene and spin coated onto cleaned sapphire substrates. The dried blends were heated at 120° C on a hotplate. The TQ1 film and TQ1:$PC_{71}BM$ 1:1 and 1:3 blends **[Paper 5]** were spin coated onto cleaned sapphire substrates.

4.2. Experimental Setup

The CELIV measurements were made in a custom built setup. The samples were mounted inside a cryostat (Oxford Instruments) and kept under vacuum. The voltage pulses and offsets were generated using a function generator (Stanford Research Systems DS345). Photogeneration of charges was made using a pulsed Nd:YAG laser (Quantel Ultra, Big Sky Laser) utilizing the second harmonic at 532 nm giving 7 ns laser pulses at a repetition rate of 1 Hz. The delay between the laser and the voltage pulses was controlled using digital delay and pulse generator (Stanford Research Systems DG535). The

current transients were recorded using a digital oscilloscope (Tektronix TDS 680B). The CELIV setup was controlled using a LabVIEW program.

In the custom built PIA setup, illustrated in Figure 4.2, the samples were mounted inside a liquid nitrogen cooled cryostat (Janis Research) and kept under vacuum. The temperature was varied using a Lakeshore temperature controller (DRC-93CA). The pump beam was supplied using an Ar-ion (Coherent Innova) laser operating at 514 nm or with a diode laser at 785 (Power Technology Inc.). The pump beam was modulated using a mechanical chopper (Stanford Research Systems) or with an acousto-optical modulator (Neos Technologies). The probe beam was obtained from a tungsten lamp. The transmitted light was collected into a monochromator (ARC SpectraPro-300i) and detected using Si, Ge and a liquid nitrogen cooled InSb photodetectors using appropriate optical filters. The detected signal from the photodetectors was amplified using pre-amplifiers (Femto DHCPA 100 or EG&G Technologies). The pre-amplified signal was measured using a phase-sensitive lock-in amplifier to obtain the PA_I and PA_Q signals.

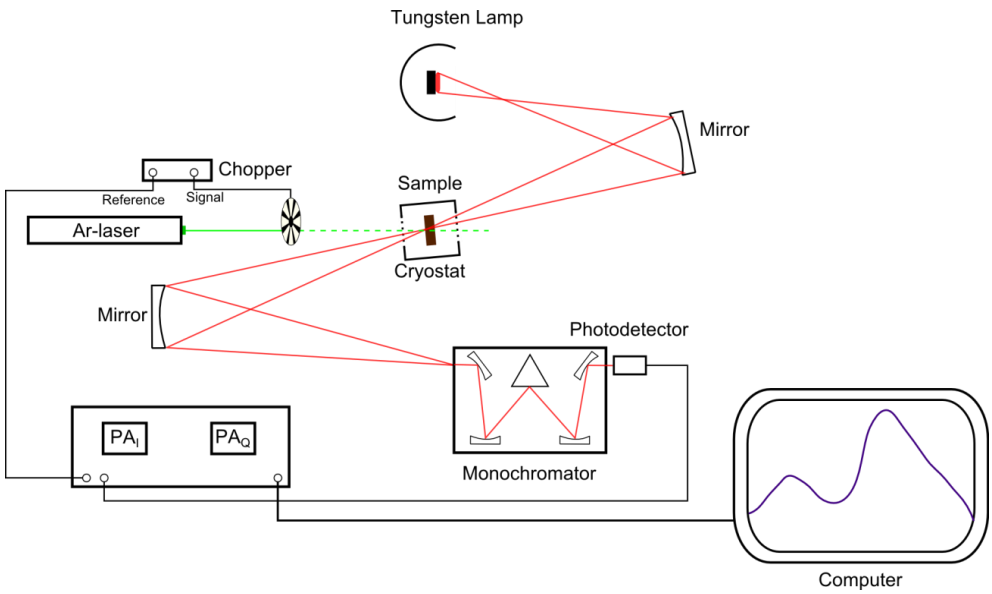

Figure 4.2. Schematic of the PIA experimental setup.

5. Results & Discussions

5.1. Injected Charge Reservoir Formation at the TiO_2/Organic Interface

In **[Paper 1]** the charge transport in hybrid TiO_2/organic devices was clarified using the CELIV technique. Devices having the structure ITO/TiO_2/P3HT:$PC_{60}BM$/Cu were characterized and compared to devices without a TiO_2 layer. The use of ITO (work function: 4.8 eV) and copper (work function: 4.7 eV) as contacts [95,96] were chosen to obtain an internal electric field close to zero at an offset voltage of 0 V, making these types of devices ideal for transport and recombination measurements.

Figure 5.1a shows a CELIV transient of a device having a 7 nm thick TiO_2 layer, where the applied offset voltage has been varied between -0.80 V and +0.80 V; note that the voltage is applied relative to the ITO. From the figure it can be seen that a large extraction current, $\Delta j > j(0)$, is obtained already at an offset voltage of -0.20 V. Furthermore, the magnitude of the extraction current increases at larger negative offsets and the maximum of the current shifts towards longer times. The behavior of a device without a TiO_2 layer is significantly different, as shown in Figure 5.1b. Here, the applied offset voltage was varied between -0.60 V and +0.60 V and, as can be seen, the extraction current is much smaller compared to the TiO_2 device in Figure 5.1a and $\Delta j < j(0)$ for all applied offsets.

The application of a negative offset voltage leads to the injection of holes at the Cu-contact. For devices with a TiO_2 layer, holes are accumulated at the TiO_2/organic interface and since TiO_2 is known to be a good hole blocker [97,98] the extraction of holes is prevented. The surface charge density of holes has been calculated for devices with a TiO_2 layer thickness of 7 nm, 14 nm and 54 nm, as well as for a device without a TiO_2 layer and is shown in Figure 5.1c.

It can be seen that the amount of surface charge for devices with a TiO_2 layer is higher than that obtained in devices without a TiO_2 layer, by around one order of magnitude. This also implies that the ITO contact is slightly hole-blocking, as an extraction current is obtained at negative offsets.

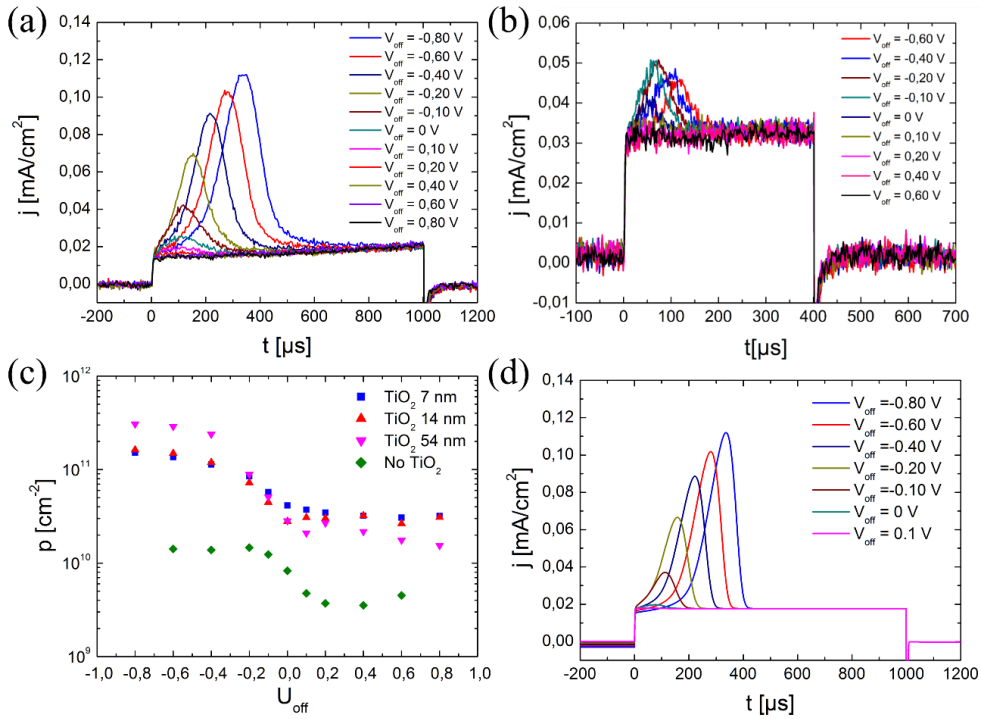

Figure 5.1. (a) CELIV current transients of a device having a 7 nm thick TiO_2 layer inserted between the ITO and the organic blend, where the offset has been varied between -0.80 V and +0.80 V, (b) transients for a device without a TiO_2 layer, where the offset voltage was varied between -0.60 V and +0.60 V, (c) the extracted surface charge as a function of the applied offset for different thicknesses of the TiO_2 layer and without a TiO_2 layer and (d) a simulated CELIV transient at different offsets between -0.80 V and +0.10 V, where the TiO_2 layer has been replaced by a reduced surface recombination rate for holes at the ITO contact.

The formation of a large hole reservoir at the TiO_2/organic interface will lead to space charge limited charge (SCLC) extraction, as shown by Juška et al. [71]. It should be pointed out that the extraction transients in other MIS-CELIV measurements overlap [71,73,75,76], while the transients here shift towards longer times as the applied offset is increased towards more negative voltages. The shift in the extraction current maximum when higher offset voltages are applied is due to the larger electric field inside the devices. To confirm that a large hole reservoir leads to SCLC extraction, modeling of the CELIV transients were performed. Simulated CELIV transients are shown in

Figure 5.1d, where the TiO_2 layer has been modeled as a reduced surface recombination rate for holes at the ITO contact. Therefore, a hole reservoir is formed at the ITO/organic interface at negative offset voltages. As can be seen from the figure, since the simulated transients reproduce the experimental results, which verify that SCLC extraction of a large hole reservoir takes place in the devices having TiO_2 interfacial layers. It should be pointed out that to the best of our knowledge the transients in **[Paper 1]** are the first SCLC transients seen in devices utilizing materials intended for use in operating solar cell devices, unlike other work where insulating layers are used to obtain the charge reservoirs [71,73,75–77].

5.1.1. Influence of an Injected Charge Reservoir on Recombination of Photogenerated Charges

The previous discussion concerned devices measured in the dark, where only one type of charge carrier (holes) is injected into the device from the contacts and subsequently extracted by the CELIV pulse. To clarify how a charge reservoir influences the charge transport and recombination in the case of photogenerated charges, photo-CELIV measurements were performed in **[Paper 2]**. The characterization was made on the same devices as in **[Paper 1]**; thus, the results in the dark and with photogeneration can be directly compared to evaluate the difference.

Photo-CELIV measurements on devices with and without a TiO_2 layer are shown in Figure 5.2 at varying excitation intensities. Transients for a device with a 7 nm TiO_2 layer at a negative offset voltage of -0.60 V is shown in Figure 5.2a. It can be seen that at low excitation intensities the transients have a similar behavior to that seen in the dark at a high negative offset voltage.

This indicates that a hole reservoir is formed at the TiO_2/organic interface, similarly to the case in the dark. By increasing the excitation intensity, the magnitude of the extraction current is increased along with a broadening of the extraction current, until saturation is observed.

The behavior at an applied offset of 0 V is shown in Figure 5.2b. In this case SCLC extraction is not observed, indicating that only a small or no charge reservoir is formed at the TiO_2/organic interface. At higer excitation intensities, the magnitude of the extraction current is increased but no broadening of the transients is observed. At positive offset voltages, most of the photogenerated charges are extracted before the application of the extraction pulse [**Paper 2**]. Nekrašas et al. [99] showed that the reduction of the bimolecular recombination ζ can be obtained from the ratio between the displacement

current $j(0)$ and the saturated extraction current Δj_{sat}. From Figure 5.2b, $\zeta = 0.007$ is obtained, which is in good agreement with other measurements [39,40,63,100].

Photo-CELIV transients for a device without a TiO_2 layer at an applied offset voltage of -0.60 V is shown in Figure 5.2c. No SCLC extraction is seen in the dark nor at low excitation intensities. However, a broadening of the extraction current transients, similar to that observed for the devices with a TiO_2 layer is seen here. Here the broadening is smaller than that seen in the TiO_2 devices. When an offset voltage of 0 V is applied, as shown in Figure 5.2d, no broadening is observed, similar to the TiO_2 device shown in Figure 5.2b. At positive offset voltages most charges are extracted prior to the application of the CELIV pulse, as was the case for the device with a TiO_2 layer.

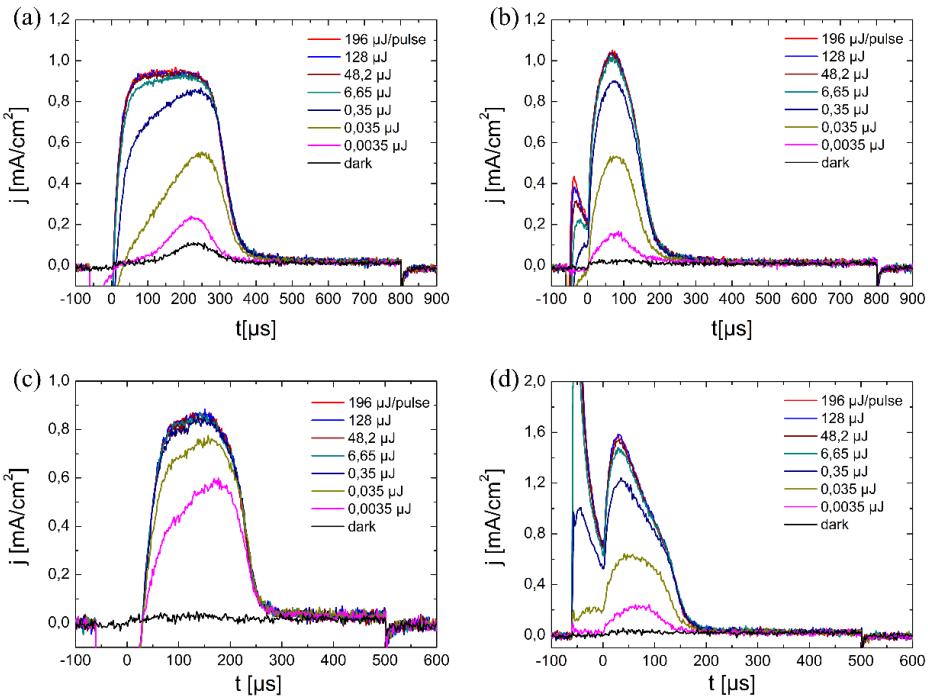

Figure 5.2. Photo-CELIV transients at increasing excitation intensities for devices with a TiO_2 layer at an applied offset voltage of (a) -0.60 V, (b) 0 V and without a TiO_2 layer at offsets of (c) -0.60 V and (d) 0 V.

To obtain insight into the charge transport and recombination behavior seen from the experimental transients in Figure 5.2, simulations of photo-CELIV transients have been performed. As mentioned earlier, the TiO_2 layer

was replaced by having a reduced surface recombination rate for holes (S_p^{an}) at the ITO contact. A reduced surface recombination velocity becomes significant when charges cannot be extracted at the contact faster than their transport to the contact [50] leading to a build-up of charges at the contact. Therefore, S_p^{an} should be larger than the effective transport velocity, v_D, which is estimated to be 0.1 cm s^{-1} in an organic semiconductor device [50,51]. The case where $S_p^{an} = 10^{-5}$ cm s^{-1} ($S_p^{an} \ll v_D$) has been simulated in Figure 5.3 at different reductions of the bimolecular recombination rate ζ, using a high density of photogenerated charges. The photogeneration (Q_L) is given in comparison to CU_0, where $U_0 = U_{off} - U_{bi}$, where U_{bi} is the built-in field and U_0 = -0.35 V. The contribution of the electron and hole extraction currents to the total photo-CELIV transient is also shown, as the dashed (electrons) and dotted lines (holes).

From Figure 5.3, it can be seen that when the recombination is Langevin ($\zeta = 1.0$) and at a low reduction $\zeta = 0.1$ a typical SCLC extraction is seen, similar to the transients in the dark. By reducing the bimolecular recombination to $\zeta = 0.01$, two extraction bumps are seen and a broadening of the extraction current is observed. At a strong reduction of the recombination ($\zeta = 0.001$), a large extraction current is seen and we note that two extraction bumps are also seen here. In addition to this, we note that the broadening of the current extraction is smaller than in the case of $\zeta = 0.01$ but the density of charges in the device is larger, as seen by the increased extraction current.

The electron and hole extraction current contributions reveal that when the recombination is close to Langevin ($\zeta = 1$ and $\zeta = 0.1$), most electrons recombine with holes before the CELIV pulse is applied. Thus only holes are left in the reservoir, leading to SCLC extraction. At a reduction of $\zeta = 0.01$, a small but significant number of electrons are left in the device, which contribute to the initial bump seen in the transient. After the electrons are extracted, the holes left in the reservoir leads to SCLC extraction. For $\zeta = 0.001$ a large number of electrons and holes are left in the reservoir, leading to a large recombination limited extraction current. From these results it can be concluded that when $\zeta \leq 0.01$, the charge extraction is space charge limited and when $\zeta = 0.001$, the extraction becomes limited by recombination in the bulk.

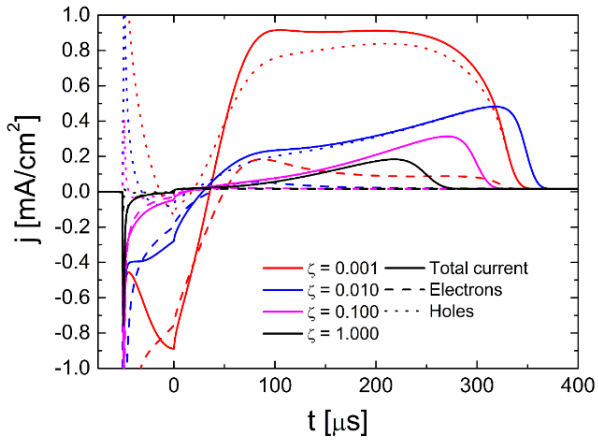

Figure 5.3. Simulated photo-CELIV transients showing the dependence on the reduction of the bimolecular recombination constant at a large amount of photogenerated charge Q_L =400× CU_0.

The magnitude of the surface recombination velocity, S_p^{an}, compared to the transport velocity, v_D, is expected to affect the extraction current transients. Figure 5.4 shows the extraction current transients at varying S_p^{an}. Simulated CELIV transients in the dark are shown in Figure 5.4a, from which it can be seen that by decreasing S_p^{an} a larger extraction current is seen as more holes are left in the reservoir at lower S_p^{an}, as expected. Photo-CELIV transients at ζ =0.001 and at high photogeneration of charges Q_L =400× CU_0 are shown in Figure 5.4b and an increased extraction current is seen when S_p^{an} is reduced. It should be noted, however, that a large extraction current is obtained at S_p^{an} =10^{-3} cm s^{-1} in contrast to the results in the dark where only a small extraction current is seen at the same surface recombination velocity. These results are in good qualitative agreement with the experimental results shown in Figure 5.2 where a large broad extraction is seen at high intensities for devices with a TiO_2 layer, while a smaller extraction current is seen for devices without a TiO_2 layer.

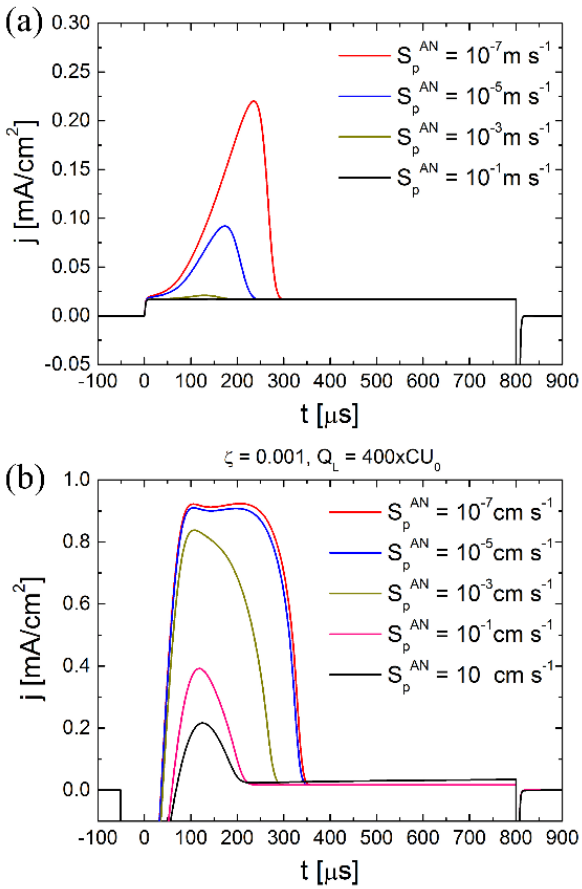

Figure 5.4 The effect of varying the surface recombination, S_p^{an}, of holes on charge transport in (a) the dark and (b) using photogeneration.

Sandberg et al. have developed a method to obtain S_p^{an} in organic devices [101]. Using this method on the device having a 7 nm TiO_2 layer, which was characterized in **[Paper 1]** and **[Paper 2]**, S_p^{an} =6×10^{-6} cm s^{-1} was obtained, which is in excellent agreement with the experimental and the simulated data in Figure 5.2 and Figure 5.3, respectively.

These results show the interplay between extraction and recombination in TiO_2/organic devices which depend on (1) the magnitude of the reduction of the recombination compared to Langevin and (2) the reduced surface recombination velocity of charges at the contacts. In addition to this, TiO_2/organic devices typically display S-shaped current-voltage ($J-V$) curves under illumination [52,102–105] which can be removed by illuminating the TiO_2 layer with ultraviolet (UV) light. The devices characterized in **[Paper 2]**

have not been UV treated and, thus, an S-shaped $J-V$ curve is expected. This is indeed what was observed in the work by Sundqvist et al. [45] where similar devices were characterized using $J-V$ and CELIV measurements. Before the UV treatment, a large charge reservoir and an S-shaped $J-V$ curve was observed. After UV treatment, a strong reduction of the charge reservoir and the S-shape disappeared.

5.2. Characterizing the Bulk Recombination in Organic BHJ Blends

To obtain the bulk recombination in solar cell devices without the influence of contacts on the recombination, the (contact free) PIA technique was used on the model system pBTTT:$PC_{60}BM$ in **[Paper 3]**. This donor:acceptor blend was chosen due to the fact that the dominating bulk recombination process can be controlled by varying the blend ratio. In 1:1 blends trap-assisted recombination has been observed, while 1:4 blends show 2D Langevin recombination [44].

The PIA spectra of pBTTT:$PC_{60}BM$ blends are shown in Figure 5.5. The 1:4 blend is shown as the red line and the 1:1 blend as the blue line. From the figure it can be seen that the intensity of the 1:4 blends is higher than in the 1:1 blend, in agreement with other work [44]. A low energy (LE) transition and several high energy (HE) transitions can be seen. The LE transition is attributed to the polaron P1 transition. The position of the P2 transition can be obtained from the relation $E_g = 2P_1 + P_2$ giving P2 = 1.21 eV [36,106].

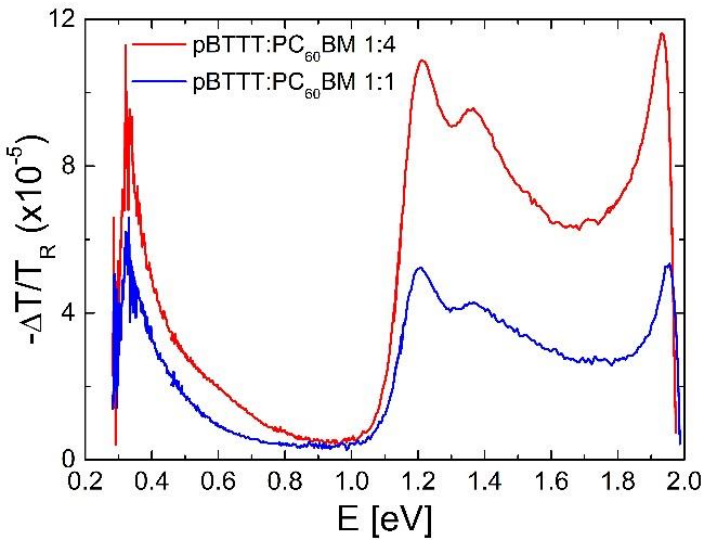

Figure 5.5. PIA spectra of pBTTT:PC_{60}BM 1:4 blend (red line) and pBTTT:PC_{60}BM 1:1 blend (blue line).

The intensity dependence of the P2 polaron transition for the pBTTT:PC_{60}BM 1:1 and 1:4 blends are shown in Figure 5.6a and Figure 5.6b, respectively. Both blends show a slope, for the in-phase (PA_I) smaller than 0.5, expected for bimolecular recombination. The slope for the 1:1 blend is 0.38 $\pm$ 0.01 and for the 1:4 blend 0.42 $\pm$ 0.02. Using Equation (3.24) the effective reaction order (δ) for the blends is 2.6 $\pm$ 0.01 and 2.4 $\pm$ 0.01, respectively. These results suggest that either trap-assisted or 2D Langevin dominates the bulk recombination, as a $\delta > 2$ is obtained in the former and $\delta = 2.5$ in the latter case.

Simulations were performed to clarify the behavior of trap-assisted recombination and 2D Langevin recombination in an intensity dependent PIA measurement. The case of trap-assisted recombination is shown in Figure 5.6c between 300K and 180 K, where the trap-depth is $E_{ch} = 45$ meV. At 300 K a slope of 0.38 is obtained, which is in good agreement with the experimental results for the 1:1 blend shown in Figure 5.6a. By lowering the temperature, a reduction of the slope can be seen, which is in good agreement with Equation (3.33). The intensity dependence of 2D Langevin recombination is shown in Figure 5.6d, where a temperature *independent* slope of 0.40 is obtained.

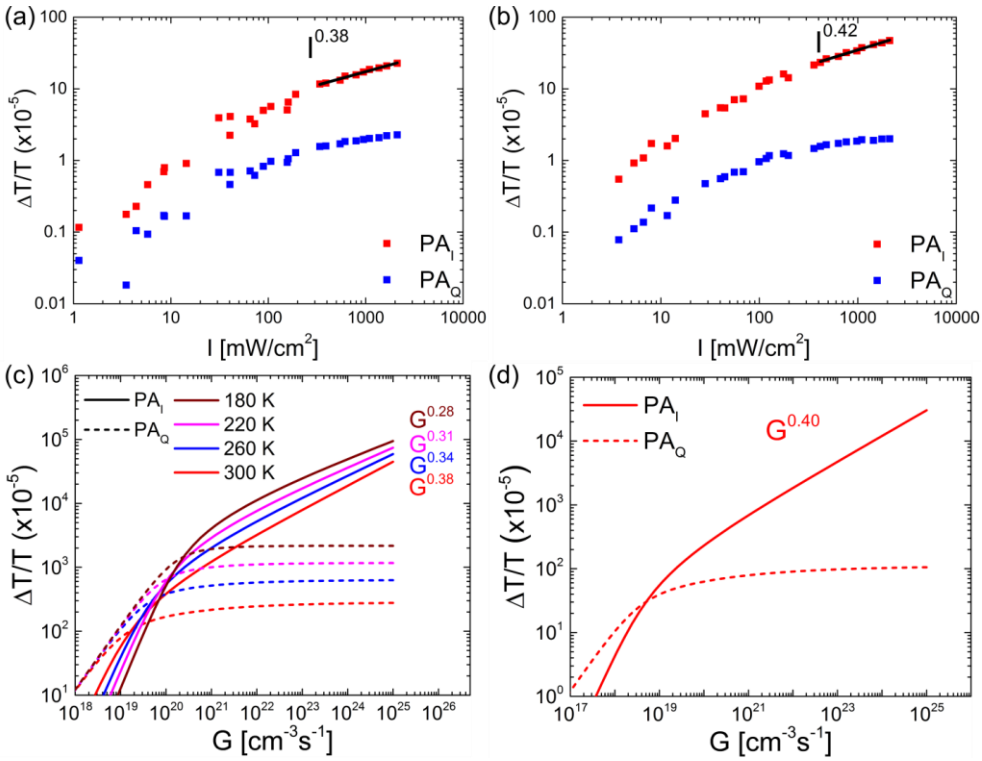

Figure 5.6. The measured intensity dependence of (a) the pBTTT:$PC_{60}BM$ 1:1 blend and (b) the pBTTT:$PC_{60}BM$ 1:4 blend and the simulated intensity dependence for (c) trap-assisted recombination having a trap-depth of E_{ch} = 45 meV and (d) 2D Langevin recombination.

The temperature dependence of the reaction order has been clarified by measuring the frequency dependence of the quadrature signal (PA_Q) between 300 K and 180 K. Using Equation (3.25) the reaction order can be obtained from the PA_Q slope at small frequencies. The frequency dependence of the 1:1 blend is shown in Figure 5.7a, where temperature dependent slopes are obtained, indicating that trap-assisted recombination dominates. The behavior of the 1:4 blend is shown in Figure 5.7b, where a very weak temperature dependence is observed. To clarify the difference between trap-assisted and 2D Langevin recombination, the PIA frequency dependence has been simulated. Trap-assisted recombination, having a trap-depth of E_{ch} = 45 meV, is shown in Figure 5.7c between 300 K and 180 K. A clear temperature dependent slope is observed, similar to that seen in the experimental results. The case of 2D Langevin recombination is shown in Figure 5.7d, where a temperature independent slope is obtained. From these results it is clear that

in the 1:1 blend, trap-assisted recombination is dominating, while 2D Langevin recombination dominates in the 1:4 blend which are in good agreement with transport measurements on similar blends made by Nyman et al. [44].

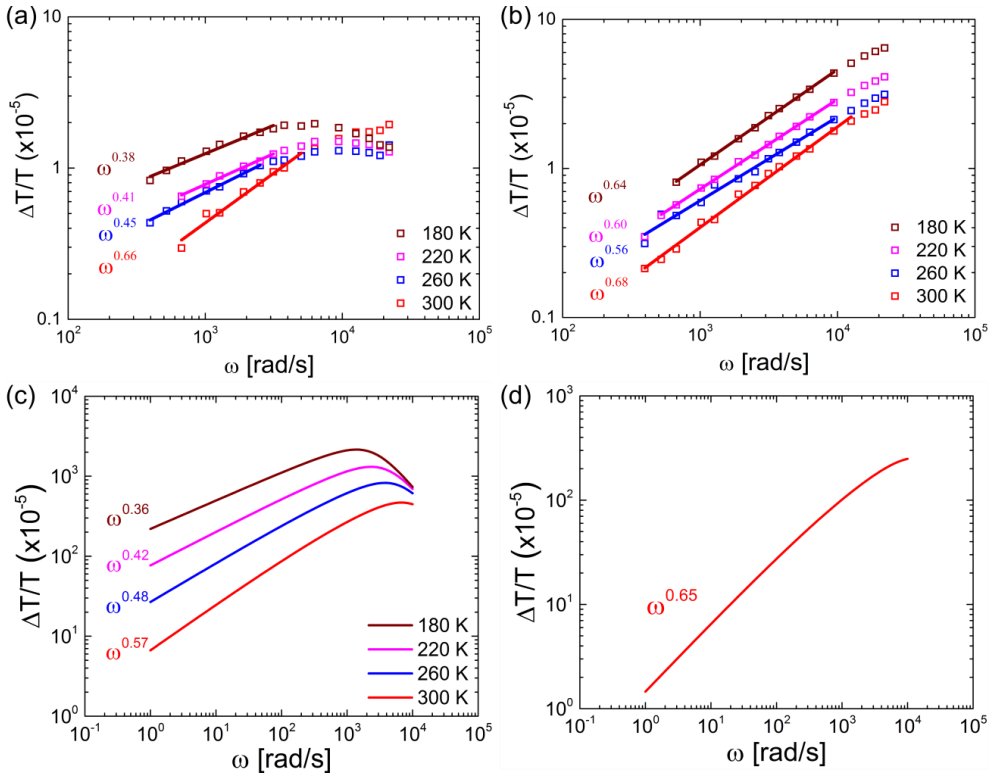

Figure 5.7. The measured frequency dependence of (a) the pBTTT:$PC_{60}BM$ 1:1 blend and (b) the pBTTT:$PC_{60}BM$ 1:4 blend and the simulated frequency dependence for (c) trap-assisted recombination having a trap-depth of E_{ch} = 45 meV and (d) 2D Langevin recombination.

The trap-depth, in the case of an exponential distribution of traps, can be determined using Equation (3.33). From the intensity dependence E_{ch} = 43±3 meV is obtained and from the frequency dependence E_{ch} = 44±5 meV. For both measurements an average of the different temperatures was used to determine E_{ch}. However, the recombination due to the 2D limited charge transport in pBTTT needs to be considered. Nyman et al. showed that in the case of 2D trap-assisted recombination $R \propto (nn_t)^{5/4}$ [44]. In this case, the reaction order will be given by $\delta_{2D} = \frac{5}{4}(1+E_{ch,2D}/kT)$. The trap depth for the intensity and frequency dependence now becomes $E_{ch,2D}$ = 31±4 meV and

$E_{ch,2D}$ = 29±2 meV, respectively. Using the PIA results alone one cannot determine whether the recombination is 2D trap-assisted or (3D) trap-assisted.

The trap depth obtained from the PIA measurements is now compared to the intensity dependent V_{oc} measurements performed by Nyman et al. on solar cells using 1:1 and 1:4 pBTTT:$PC_{60}BM$ blends [44]. The V_{oc} depends on the light intensity via the following relation [44,47,107,108]:

$$V_{oc} = n_{id}\frac{kT}{q}\ln\left(I_{light}\right) + \text{constant}, \tag{5.1}$$

where q is the elementary charge, I_{light} the light intensity and n_{id} is the light ideality factor. The light ideality factor is related to the reaction order for *free carriers*, α, by $n_{id} = 2/\alpha$. The reaction order for free carriers, in the case of (3D) trap-assisted recombination, is given by: $\alpha = 1 + kT/E_{ch}$ [44,46,47] and for 2D trap-assisted by $\alpha_{2D} = \frac{5}{4}(1+kT/E_{ch,2D})$. The measured light ideality factor of the pBTTT:$PC_{60}BM$ 1:1 blend was n_{id} = 1.15 [44]. By using E_{ch}, in the case of (3D) trap-assisted recombination obtained from the PIA measurements, light ideality factors of n_{id} =1.24±0.03 and n_{id} =1.26±0.05 are obtained for the intensity and frequency dependence, respectively. These results are in good agreement with the PIA results, noting that the difference between the PIA and the measured n_{id} can be due to surface recombination [50–52,109,110]. If 2D trap-assisted recombination dominates, the light ideality factor becomes $n_{id} = 0.85 \pm 0.03$ and $n_{id} = 0.87 \pm 0.05$, using the intensity and frequency dependence, respectively, which is in clear disagreement with the measured n_{id}. Hence, it can be concluded that the recombination in the 1:1 blends is dominated by (3D) trap-assisted recombination.

The PIA results for the 1:4 blends are also compared to the measured light ideality factor. From the intensity and frequency dependence the reaction order was δ = 2.4±0.01 and δ = 2.6±0.01, respectively. The corresponding ideality factors are now n_{id} = 0.83±0.01 and n_{id} = 0.77±0.03. The measured light ideality factor was n_{id} = 0.87 [44], which is in good agreement with the values obtained from the PIA measurements. These results show that PIA measurements can be used to determine the reaction order in organic materials and blends and in the case of trap-assisted recombination the trap-depth can be obtained.

5.2.1. Influence of a Large and Small Interfacial Dipole on Recombination in Ordered P3HT:fullerene Blends

Interfacial dipoles have been observed in BHJ blends at the donor/acceptor interface. Interfacial dipoles of $\Delta = 0.5\text{-}0.6$ eV [111] and $\Delta = 0.3\text{-}0.4$ eV [112] were observed at the P3HT/$PC_{60}BM$ and P3HT/ICBA interface, respectively, using ultraviolet electron spectroscopy (UPS) and inverse photoemission spectroscopy (IPES). By analyzing UPS measurements at the P3HT/$PC_{60}BM$ interface using the integer charge transfer (ICT) model, an interfacial dipole of $\Delta = 0.4$ eV was observed by Xu et. al. [113] and $\Delta = 0.31$ eV by Bao et. al., while a small interfacial dipole $\Delta = 0.05$ eV was observed at the P3HT/ICBA interface [60]. Hence, by using the methods shown in [**Paper 3**], PIA measurements are utilized in **[Paper 4]** to clarify if a larger interfacial dipole leads to more trap-assisted recombination in P3HT:$PC_{60}BM$ blends compared to P3HT:ICBA.

The PIA spectra of annealed 1:1 blends of P3HT:ICBA and P3HT:$PC_{60}BM$ are shown in Figure 5.8 as the red and blue lines, respectively, using the above gap excitation at 2.41 eV. The shape of the spectra is similar between both blends: a low energy (LE) transition is seen at 0.33 eV which is assigned to be due to the P1 polaron transition and two high energy (HE) transitions are observed at 1.26 eV and 1.81 eV, respectively. These HE transitions are due to the localized (P2) and delocalized polaron (DP2), which is in good agreement with other work [35,59,114,115]. The density of polarons generated in the blends has been estimated using Equation (3.1), where the thick film approximation has been assumed due to the high absorption coefficient at this excitation energy, and the result is shown in Table 5.1. The density of the P2 transition is similar between the two blends, while a slightly higher density of DP2 is seen in P3HT:$PC_{60}BM$ blends.

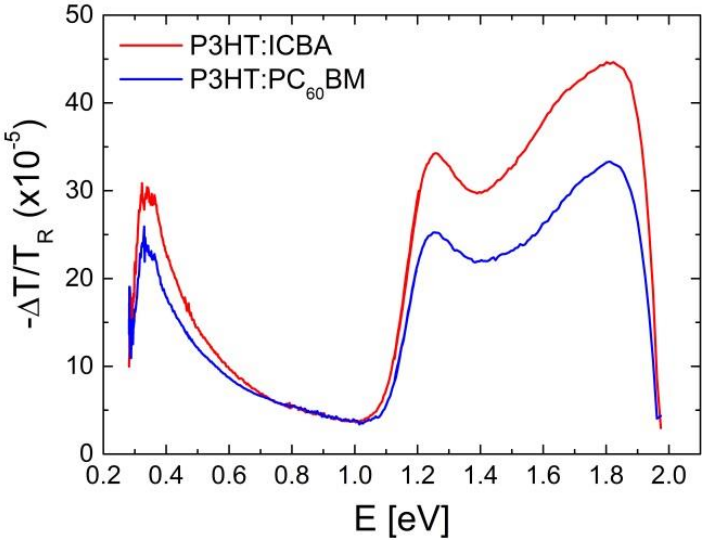

Figure 5.8. The PIA spectra obtained using above gap excitation at 2.41 eV of P3HT:ICBA (red line) and P3HT:$PC_{60}BM$ (blue line)

To clarify if a larger interfacial dipole leads to more trap-assisted recombination, as suggested by Bao et al. [60], the recombination in the two blends was characterized using intensity dependent measurements. The intensity dependence of the P2 transition is shown for P3HT:ICBA and P3HT:$PC_{60}BM$ in Figure 5.9a and Figure 5.9b, respectively. From the figure it can be seen that the slope is 0.48±0.01, for both blends, yielding a reaction order of $\delta = 2.08 \pm 0.04$. Using Equation (3.33), the mean trap-depth is obtained as $E_{ch} = 28.0 \pm 1.1$ meV. The intensity dependence of the DP2 transition is shown in Figure 5.9c and Figure 5.9d for P3HT:ICBA and P3HT:$PC_{60}BM$, respectively. The same slope of 0.48±0.01 is also obtained in this case, resulting in the same trap-depth of $E_{ch} = 28.0 \pm 1.1$ meV. The obtained trap-depths are close to the thermal energy at room temperature (26 meV). When $E_{ch} \approx kT$, the traps will not contribute to trap-assisted recombination and bimolecular recombination will dominate [48,49]. A temperature dependent reaction order will conclusively show that trap-assisted recombination dominates.

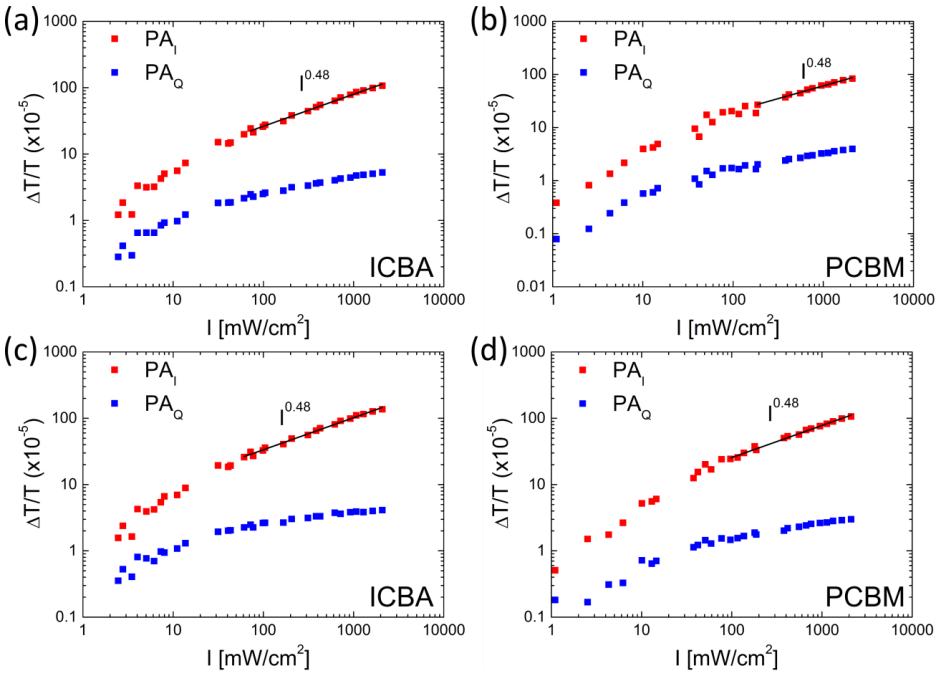

Figure 5.9. The intensity dependence of P3HT:ICBA and P3HT:PC$_{60}$BM, excited at 2.41 eV for the (a)-(b) P2 transition and (c)-(d) DP2 transition.

Frequency dependent measurements between 300 K and 180 K are shown in Figure 5.10a and Figure 5.10b for P3HT:ICBA and P3HT:PC$_{60}$BM, respectively. The effective reaction order was obtained from the slope of the quadrature component at low frequencies using Equation (3.25). The slopes can be seen to have a weak temperature dependence, noting that the P3HT:ICBA blend shows a slightly stronger temperature dependence compared to the P3HT:PC$_{60}$BM blend. For the DP2 transition, the frequency dependence is shown in Figure 5.10c and Figure 5.10d for P3HT:ICBA and P3HT:PC$_{60}$BM, respectively. Here, it can be seen that both blends exhibit very weak temperature dependence. The trap-depth can now be determined from the frequency dependence using Equation (3.33). To avoid errors due to the trap-depth E_{ch} being close to kT [49], the estimation of E_{ch} was made at 180 K and is given in Table 5.1. The trap-depths for the P2 transition are E_{ch}=24.4$\pm$0.7 meV and E_{ch}=21.3$\pm$0.3 for P3HT:ICBA and P3HT:PC$_{60}$BM, respectively. For the DP2 transition, the trap-depths are E_{ch}=20.5$\pm$0.2 meV for P3HT:ICBA and E_{ch}=22.4$\pm$0.3 meV for P3HT:PC$_{60}$BM. From these results, the temperature independent behavior near 300 K and the obtained trap-depths being lower than 26 meV, we conclude that bimolecular recombination is the

dominating bulk recombination mechanism in both blends at room temperature.

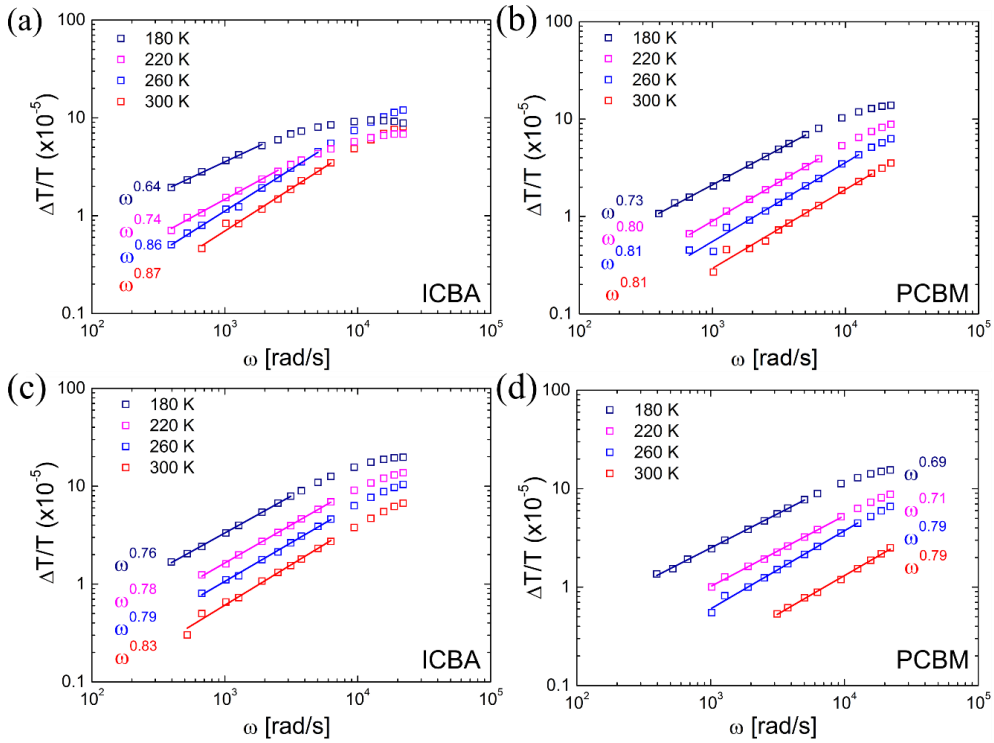

Figure 5.10. The frequency dependence of the quadrature signal between 300 K and 180 K for the P2 transition of (a) P3HT:ICBA and (b) P3HT:$PC_{60}BM$ and the DP2 transition for (c) P3HT:ICBA and (d) P3HT:$PC_{60}BM$, using an excitation intensity of 100 mW/cm^2.

Since bimolecular recombination dominates at 300 K, the bimolecular recombination constant can now be determined from the intensity dependence of the quadrature component, using Equation (3.15). Bimolecular recombination yields a straight line and the slope will be given by $\omega\sigma d/2\pi\beta$ [91]. The intensity dependence of the quadrature component for the P2 transition is shown in Figure 5.11a and for the DP2 transition in Figure 5.11b for P3HT:ICBA (filled red squares) and P3HT:$PC_{60}BM$ (open blue squares). A clear difference can be seen between the P2 and DP2 transitions. Two different slopes can be seen for the P2 transition, one at low intensities and another at high intensities, while the same slope is observed over most of the intensity range for the DP2 transition. This suggests that trap-assisted recombination dominates at low intensities for the P2 transition and

bimolecular recombination dominates at high intensities, but for the DP2 transition, bimolecular recombination is dominating over the whole intensity range probed. This result is in good agreement with Guo et al. [116] who observed trap-limited bimolecular recombination for the P2 transition and (trap-free) bimolecular recombination for the DP2 transition.

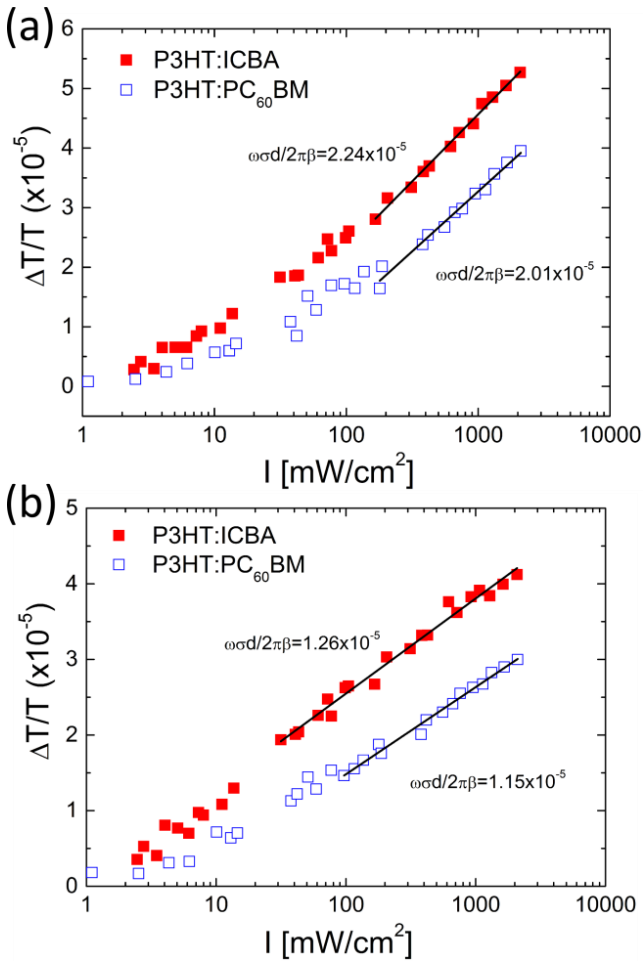

Figure 5.11. The intensity dependence of the quadrature component for (a) the P2 transition and (b) the DP2 transition, where P3HT:ICBA is shown as the filled red squares and P3HT:PC_{60}BM as the open blue squares.

The bimolecular recombination constants obtained from Figure 5.11 using equation (3.15) is given in Table 5.1. To compare the bimolecular recombination constants between the two blends, the ratio between the bimolecular recombination constant and the mobility (β/μ) is determined. The mobility was obtained using photo-CELIV measurements and is shown

in Table 5.1. By obtaining the β/μ ratio, the effect the charge transport has on the recombination can be reduced [117]. For the DP2 transition the β/μ ratio has similar values, indicating the same recombination between the two blends. For the P2 transition, the β/μ ratio is higher in the P3HT:ICBA blends by a factor of 2. Interfacial dipoles are expected to be located in the amorphous region of the blend [59], which is also where the localized polarons are located. Therefore, interfacial dipoles are expected to have the greatest effect on the recombination of the localized polarons. However, the β/μ ratio is also affected by the bimolecular recombination coefficient [59]. Since a larger reduction of the bimolecular recombination is observed in P3HT:$PC_{60}BM$ blends after annealing, this reduction is affected by the morphology of the blend. Morphological characterization of the P3HT:ICBA and P3HT:$PC_{60}BM$ blends have shown clear differences between the blends [118,119], and it is also expected that the reduction of the bimolecular recombination is different between the two blends.

Measurements of the light ideality factor on P3HT:ICBA and P3HT:$PC_{60}BM$ [107] blends have suggested that trap-assisted recombination is more pronounced in P3HT:$PC_{60}BM$ blends. The PIA technique reveals the dominating bulk recombination and is not affected by surface recombination at the contacts. Since only a small difference in the β/μ ratio was observed between the blends, it is concluded that interfacial dipoles have little or no effect on the bulk recombination in P3HT:fullerene blends.

Table 5.1. The parameters evaluated for the localized polaron (P2) and delocalized polaron (DP2) transitions. The mobility was obtained using photo-CELIV.

	P3HT:ICBA		**P3HT:$PC_{60}BM$**	
	P2 (1.26 eV)	DP2 (1.80 eV)	P2 (1.26 eV)	DP2 (1.80 eV)
n_{514} [cm^{-3}]	1.12(±0.04)x10^{17}	1.49(±0.01) x10^{17}	1.10(±0.01)x10^{17}	1.64(±0.01) x10^{17}
E_{ch} [meV]	24.4(±0.7)	20.5(±0.2)	21.3(±0.3)	22.4(±0.3)
β [cm^3s^{-1}]	8.8(±0.3)x10^{-14}	15.8(±0.5) x10^{-14}	7.4(±0.3)x10^{-14}	17.2(±0.5)x10^{-14}
μ [$cm^2V^{-1}s^1$]	5.0(±1.0)x10^{-4}		8.0(±2.0)x10^{-4}	
β/μ [Vcm]	1.8(±0.4)x10^{-10}	3.2(±0.6)x10^{-10}	0.9(±0.2)x10^{-10}	2.2(±0.6)x10^{-10}

5.2.2. Recombination in Amorphous TQ1:$PC_{71}BM$ Blends with a Small Interfacial Dipole

Similarly to the P3HT:ICBA blends in [**Paper 4**], the TQ1:$PC_{71}BM$ blends should also have an interfacial dipole of $\Delta = 0$ eV according to Bao et al. [60], however, these blends show a different morphology in comparison to P3HT blends, with TQ1 blends being amorphous [120]. To clarify the influence of morphology in blends with a small or no interfacial dipole in **[Paper 5]** we use the PIA technique to obtain the dominating recombination type in TQ1:$PC_{71}BM$ blends. Films of TQ1 and TQ1:$PC_{71}BM$ blends with a blend ratio of 1:1 and 1:3 were characterized. The 1:1 and 1:3 blend ratios were chosen, as 1:3 blends typically show the highest solar cell PCE [121,122]

The PIA spectra at 80 K are shown in Figure 5.12a. For the TQ1 film, shown as the red line, an intense peak is seen at 1.0 eV, which is attributed to triplet absorption since no low energy peaks, indicating polarons, can be seen. In the TQ1:$PC_{71}BM$ 1:1 blend (blue line), a LE peak is seen at 0.34 eV, which is attributed to the P1 polaron transition, the triplet transition is blue shifted compared to the TQ1 film, having a peak at 1.06 eV and the magnitude of the peak is reduced. For the TQ1:$PC_{71}BM$ 1:3 blend, shown as the magenta line, a further blue shift of the triplet peak to 1.09 eV is seen as well as a further reduction of the magnitude of the peak. From the phase spectra shown in Figure 5.12b the TQ1 exhibits a constant phase between 1.1 eV and 0.8 eV while the phase increases below 0.7 eV. The reason for the increased phase, might be due to a small number of polarons in the film. For the 1:1 and 1:3 blends, three different phases can be seen in the spectra: one at 0.4 eV, another between 0.9 eV and 1.1 eV, and another at 1.2 eV. The phase confirms that the peak at 0.33 eV and around 1.0 eV is due to two different photoexcitations. The different phase at 1.2 eV, suggest that the blue shift of the triplet absorption seen in the spectra of the blends is due to a superposition of the triplet and P2 transition peaks.

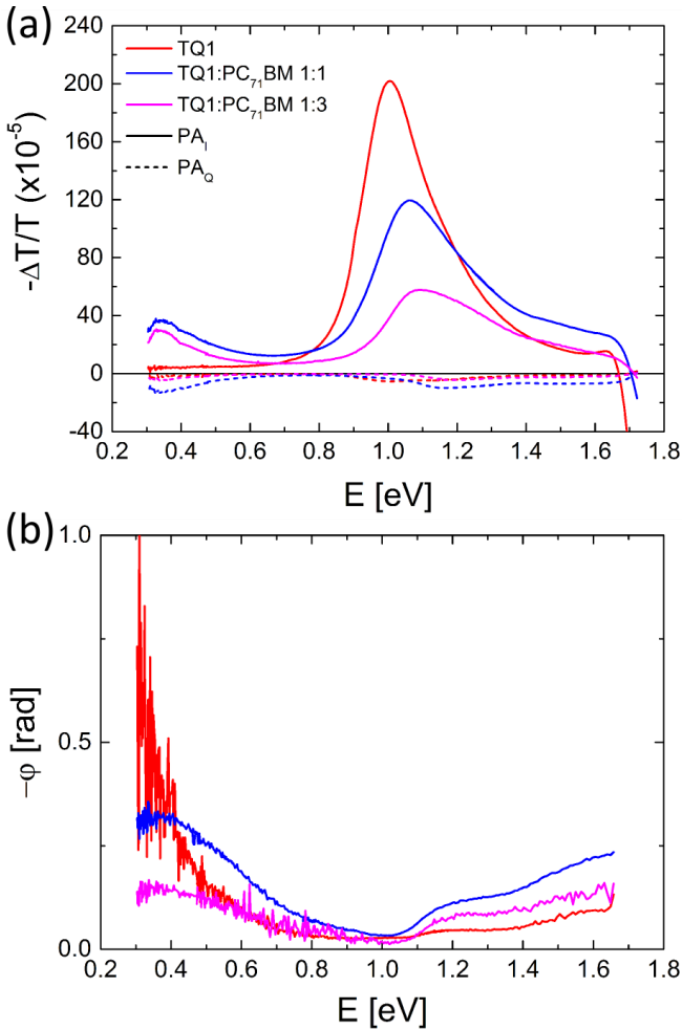

Figure 5.12. The (a) PIA spectra of TQ1 (red line), TQ1:PC$_{71}$BM 1:1 (blue line) and TQ1:PC$_{71}$BM 1:3 (magenta line), where PA_I and PA_Q are shown as the solid and dashed lines, respectively, and (b) the phase spectra measured at 80 K using excitation at 2.41 eV.

From the PIA spectra at 300 K, shown in Figure 5.13a for the TQ1 film, shown as the red line, a LE transition at 0.34 eV and a HE transition at 1.08 eV are seen, which are attributed to the P1 and triplet absorption, respectively. The HE transition is attributed to be due to triplet absorption and not to the P2 polaron transition since the energetic position of the transition is similar to that seen at 80 K and the intensity of the HE transition is much larger than the LE transition. For the 1:1 and 1:3 blends, the intensity of the P1 transition at 0.34 eV is increased as the polaron generation becomes more efficient in the

blends and the HE peaks at 1.16 eV and 1.20 eV, for the 1:1 and 1:3 blends, respectively, are attributed to the P2 transition. The phase spectra in Figure 5.13b shows a similar value over most of the energy range, however, the noisy phase signal makes drawing any conclusions difficult.

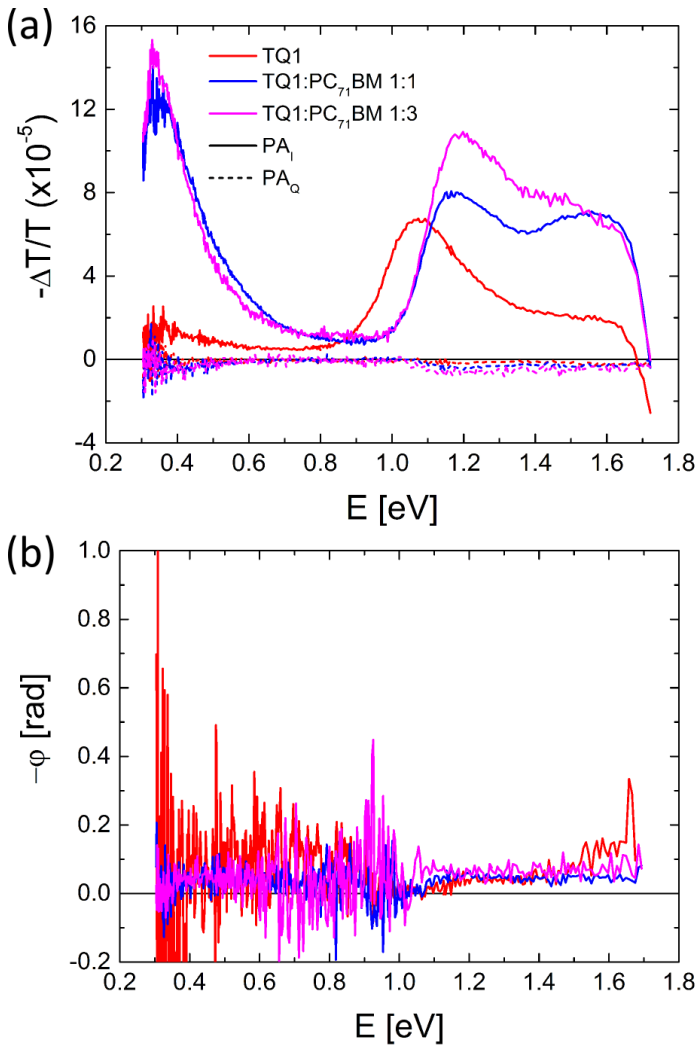

Figure 5.13. The (a) PIA spectra of TQ1 (red line), TQ1:PC$_{71}$BM 1:1 (blue line) and TQ1:PC$_{71}$BM 1:3 (magenta line), where PA_I and PA_Q are shown as the solid and dashed lines, respectively, and (b) the phase spectra measured at 300 K using excitation at 2.41 eV.

The intensity dependence of the P2 transition for TQ1:$PC_{71}BM$ 1:1 and TQ1:$PC_{71}BM$ 1:13 is shown in Figure 5.14a and Figure 5.14b, respectively. Both blends have a slope at high intensities lower than what is expected for bimolecular recombination. The slope for the 1:1 blend is 0.40 ± 0.01, equivalent to an effective reaction order of 2.50 ± 0.08. A trap depth of E_{ch} =38.7±2.0 meV is now obtained. For the 1:3 blend the slope is 0.35±0.01, resulting in an effective reaction order of 2.86±0.08 leading to a trap-depth of E_{ch} = 48.4±2.0 meV, a slightly higher trap-depth than in the 1:1 blends. While the effective reaction order in the 1:1 blend is 2.50, which would be expected for 2D Langevin recombination, this is only seen in blends showing a high ordering of the polymer **[Paper 3]** [44,123] and since no high ordering of the TQ1 polymer has been observed [120], it is concluded that trap-assisted recombination dominates in both blends.

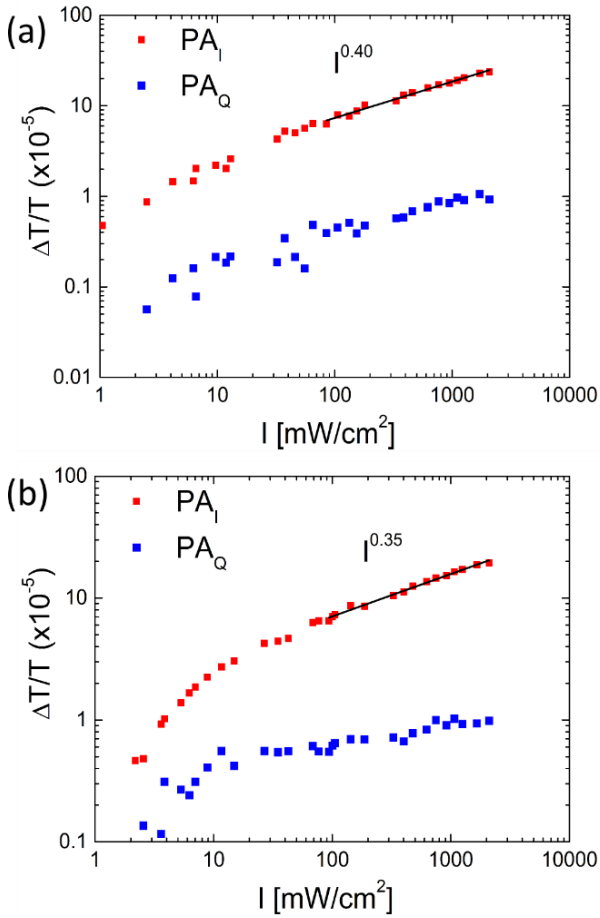

Figure 5.14. The intensity dependence of the P2 transition of the TQ1:$PC_{71}BM$ (a) 1:1 and (b) 1:3 blends, measured at 300 K using 2.41 eV excitation.

The observation of triplet absorption in the TQ1:$PC_{71}BM$ blends shown Figure 5.12 has been suggested to act as a loss mechanism in solar cells blends. While triplets can be formed by intersystem crossing of the initially generated singlet excitons, Vithanage et al. observed no triplets using transient absorption measurements [124] and in addition to this the photoluminescence is strongly quenched in the blends, making the formation of triplets from singlet excitons unlikely. Another pathway for triplet formation is recombination via the CT state. This can occur if the triplet state lies more than 0.1 eV below the CT state [29,34]. The energy of the CT state has been shown to lie around 1.5 eV [125,126] while the triplet state is located at 1.05 eV [127], indicating that triplets are formed due to charge recombination via the CT state. An energy diagram of the photoexcitations in the TQ1:$PC_{71}BM$ blends is shown in Figure 5.15.

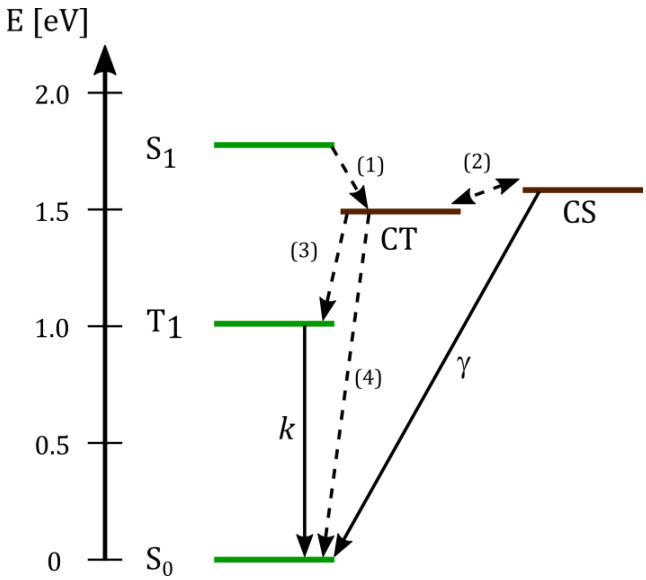

Figure 5.15. Energy diagram of the photoexcitations in the TQ1:$PC_{71}BM$ blends. S_0 is the ground state, S_1 and T_1 the lowest singlet and triplet state, respectively, CT the charge transfer state and CS the charge separated state. The decay pathways observed in this work are marked as the solid lines: k decay of the triplet state (Equation 16) and γ: recombination of the CS state, the coupling between the triplet and the CS state is given by γ_{TPA} (see main text for details). Also included as the dashed lines are the: (1) singlet exciton dissociation to the CT state, (2): dissociation/recombination between the CT and the charge separated state, (3): decay of the CT state into the triplet state, (4): direct decay of the CT state.

6. Summary

In this work, charge extraction and photoinduced absorption measurements have been applied on a variety of photovoltaic blends and devices to characterize the charge transport and recombination behavior of injected and photogenerated charge carriers. In devices having a hole blocking TiO_2 layer between the organic material and the ITO contact, we show, using the CELIV technique, that a large injected hole reservoir is formed at the TiO_2/organic interface which leads to space charge limited current extraction.

The influence an injected charge reservoir has on the charge transport and recombination of photogenerated charge carriers was clarified using photo-CELIV. When charges are photogenerated, SCLC extraction is observed at low excitation intensities. At higher intensities, a charge reservoir of both electrons and holes is formed at the interface, leading to a broadening of the extraction current. By modeling the transients, it is shown that a large reduction of the Langevin bimolecular recombination constant is needed to form the electron and hole reservoir and a qualitative estimation of the reduced surface recombination velocity of holes at the ITO/TiO_2 contact is obtained. These results show a complex interplay between injected and photogenerated charge carriers which depend on the reduced surface recombination velocity for holes and the magnitude of the reduced bimolecular recombination constant.

Using the PIA technique, it is shown how to determine the dominating recombination type in the model system pBTTT:$PC_{60}BM$, where the recombination is trap-assisted in 1:1 blends and 2D Langevin in 1:4 blends. Using intensity and frequency dependent measurements along with simulations, we show how to distinguish between free carrier and trap-assisted recombination. In the case of an exponential distribution of traps, the characteristic energy, describing the mean trap depth is obtained. The obtained results are compared to other measurements in the literature, showing a good agreement with the obtained results.

The blends P3HT:$PC_{60}BM$ and P3HT:ICBA have been shown to have a large and small interfacial dipole at the P3HT/fullerene interface, respectively. By applying the PIA technique on these blends to obtain the dominating recombination mechanism, we show that bimolecular recombination dominates in both blends. By determining the bimolecular recombinant constant in both blends for the localized and delocalized polaron, it is

determined that an interfacial dipole shows little or no influence on the recombination mechanism in these blends.

The donor-acceptor polymer TQ1 in blends with $PC_{71}BM$ has an amorphous morphology and no interfacial dipole. Using PIA measurements, triplets are observed at 80 K and are suggested to act as a loss mechanism in solar cell devices. At 300 K, the dominating recombination mechanism is shown to be trap-assisted. The trap-depth is obtained from the intensity dependence and shown to be of 38.7 meV in the 1:1 blends and of 48.4 meV in the 1:4 blends.

Svensk Resumé

I detta arbete har laddningsextraktion och fotoinducerad absorbans mätningar använts för att klargöra laddningstransporten och rekombinationen av injicerade och fotogenererade laddningsbärare i flera olika material ämnade för tillämpning i organiska solceller. I solceller som har ett hålblockerande titandioxidlager (TiO_2) mellan det organiska lagret och indium tennoxidlagret (ITO) har vi visat, med hjälp CELIV tekniken att en stor injicerad hålreservoar bildas vid det TiO_2/organiska gränsytan. Genom att använda CELIV tekniken har vi kunnat visa att detta ledder till rymdladdningsbegränsad laddningsextraktion.

Den påverkan en injicerad laddningsreservoar har på laddningstransporten och rekombinationen på fotoinducerade laddningsbärare har klargjorts med hjälp av foto-CELIV tekniken. Då fotoinducerade laddningsbärare skapas med låg exciteringsintensitet leder det till rymdladdningsbegränsad laddningsextraktion. Vid högre exciteringsintensiteter skapas en stor laddningsreservoar vid gränsytan. Denna reservoar består av både elektroner och hål, vilket leder till en breddning av extraktionsströmmen. Genom matematisk modellering av extraktionstransienterna, visar vi att en stor minskning av den bimolekylära rekombinationskonstanten leder till en reservoar som består av både elektroner och hål. Med hjälp av denna matematiska modell har vi erhållit en kvalitativ uppskattning av hastigheten för ytladdningsrekombination av hål vid ITO/TiO_2 kontakten. Dessa resultat visar att ett komplicerat samspel mellan injicerade och fotogenerade laddningsbärare pågår i laddningsreservoaren. Detta samspel påverkas av hastigheten för ytladdningsrekombination av hål och minskningen på den bimolekylära rekombinationskonstanten.

Fotoinducerad absorbans tekniken har använts för att bestämma den dominerande rekombinationstypen i modellsystemet pBTTT:$PC_{60}BM$. I detta system påverkas rekombinationen av fällor då blandningsförhållandet är 1:1 och påverkas av tvådimensionell Langevin rekombination i 1:4 förhållandet. Genom att använda intensitets- och frekvensberoende mätningar, visar vi hur man kan skilja åt då rekombinationen begränsas av fällor och då den beror på tvådimensionell Langevin rekombination. I det fall då fällorna kan beskrivas av en exponentiell fördelning visas det att den karakteristiska energin, vilken beskriver medeldjupet på fällorna, kan fås från dessa mätningar. De uppmätta resultaten har jämförts med andra mätningar från litteraturen och visar sig överensstämma bra med våra resultat.

Solcells blandningen P3HT:$PC_{60}BM$ har visat sig ha en stor dipol vid P3HT/$PC_{60}BM$ gränsytan, medan en liten dipol vid gränsytan har observerats i P3HT:ICBA blandningar. Genom att använda fotoinducerad absorbans mätningar på dessa olika blandningar, visar vi att bimolekylär rekombination dominerar i båda blandningarna. Genom att bestämma värdet på den bimolekylär rekombinationskonstanten för båda blandningarna, för både den lokaliserade och den delokaliserade polaronen, visar vi att en dipol vid gränsytan har ingen, eller endast en liten påverkan på rekombinationen i dessa solcells blandningar.

Donator-acceptor polymeren TQ1 har en amorf morfologi i blandningar med $PC_{71}BM$ och ingen dipol vid gränsytan. Med hjälp av fotoinducerad absorbans mätningar, har vi observerat triplett absorption vi 80 K. Vi föreslår att tripletterna kan agera som en förlustmekanism i organiska solceller. Vid 300 K påverkas rekombinationen av fällor och djupet på fällorna har uppskattas vara 38.7 meV i 1:1 blandningarna och 48.4 meV i 1:4 blandningarna.

References

[1] International Energy Agency, *Technology Roadmap: Solar Photovoltaic Energy - 2014 edition*, http://www.iea.org/publications/, (Accessed 15.02.2018).

[2] D. M. Chapin, C. S. Fuller, and G. L. Pearson, J. Appl. Phys. **25**, 676 (1954).

[3] R. L. Easton and M. J. Votaw, Rev. Sci. Instrum. **30**, 70 (1959).

[4] NASA Space Science Data Coordinated Archive, *Vanguard I*, https://nssdc.gsfc.nasa.gov/, (Accessed 17.10.2017).

[5] NASA Planetary Science Division, *Basics of Spaceflight*, https://solarsystem.nasa.gov/basics/, (Accessed 17.10.2017).

[6] US Energy Information Administration, *Renewable Energy Production and Consumpion by Source*, https://www.eia.gov/renewable/ (Accessed 17.10.2017).

[7] J. Yan and B. R. Saunders, RSC Adv. **4**, 43286 (2014).

[8] S. D. Collins, N. A. Ran, M. C. Heiber, and T. Q. Nguyen, Adv. Energy Mater. **7**, 1602242 (2017).

[9] C. Deibel and V. Dyakonov, Reports Prog. Phys. **73**, 96401 (2010).

[10] M. A. Green, K. Emery, Y. Hishikawa, W. Warta, E. D. Dunlop, D. H. Levi, and A. W. Y. Ho-Baillie, Prog. Photovoltaics Res. Appl. **25**, 3 (2017).

[11] M. Jørgensen, K. Norrman, and F. C. Krebs, Sol. Energy Mater. Sol. Cells **92**, 686 (2008).

[12] C. W. Tang, Appl. Phys. Lett. **48**, 183 (1986).

[13] S. F. Alvarado, P. F. Seidler, D. G. Lidzey, and D. D. C. Bradley, Phys. Rev. Lett. **81**, 1082 (1998).

[14] V. I. Arkhipov and H. Bässler, Phys. Status Solidi A **201**, 1152 (2004).

[15] J.-L. Brédas, J. Cornil, and A. J. Heeger, Adv. Mater. **8**, 447 (1996).

[16] T. M. Clarke and J. R. Durrant, Chem. Rev. **110**, 6736 (2010).

[17] T. Stübinger and W. Brütting, J. Appl. Phys. **90**, 3632 (2001).

[18] P. E. Shaw, A. Ruseckas, and I. D. W. Samuel, Adv. Mater. **20**, 3516 (2008).

[19] N. S. Sariciftci, L. Smilowitz, A. J. Heeger, and F. Wudi, Science **258**, 1474 (1992).

[20] G. Yu, J. Gao, J. C. Hummelen, F. Wudl, and A. J. Heeger, Science **270**, 1789 (1995).

[21] X. Yang, J. Loos, S. C. Veenstra, W. J. H. Verhees, M. M. Wienk, J. M. Kroon, M. A. J. Michels, and R. A. J. Janssen, Nano Lett. **5**, 579 (2005).

[22] S. R. Forrest, MRS Bull. **30**, 28 (2005).

[23] P. Würfel, *Physics of Solar Cells* (Wiley-VCH, Weinheim, 2005), p. 27.

[24] Y. Huang, E. J. Kramer, A. J. Heeger, and G. C. Bazan, Chem. Rev. **114**, 7006 (2014).

[25] J. Guo, H. Ohkita, H. Benten, and S. Ito, J. Am. Chem. Soc. **131**, 16869 (2009).

[26] A. Köhler and H. Bässler, Mater. Sci. Eng. R **66**, 71 (2009).

[27] A. Köhler, J. S. Wilson, R. H. Friend, M. K. Al-Suti, M. S. Khan, A. Gerhard, and H. Bässler, J. Chem. Phys. **116**, 9457 (2002).

[28] A. Köhler and D. Beljonne, Adv. Funct. Mater. **14**, 11 (2004).

[29] D. Veldman, S. C. J. Meskers, and R. A. J. Janssen, Adv. Funct. Mater. **19**, 1939 (2009).

[30] C. Piliego and M. A. Loi, J. Mater. Chem. **22**, 4141 (2012).

[31] M. A. Faist, T. Kirchartz, W. Gong, R. S. Ashraf, I. McCulloch, J. C. De Mello, N. J. Ekins-Daukes, D. D. C. Bradley, and J. Nelson, J. Am. Chem. Soc. **134**, 685 (2012).

[32] K. Vandewal, S. Albrecht, E. T. Hoke, K. R. Graham, J. Widmer, J. D. Douglas, M. Schubert, W. R. Mateker, J. T. Bloking, G. F. Burkhard, A. Sellinger, J. M. Frechet, A. Amassian, M. K. Riede, M. D. McGehee, D. Neher, and A. Salleo, Nat. Mater. **13**, 63 (2014).

[33] M. Pope and C. E. Swenberg, *Electronic Processes in Organic Crystals and Polymers* (Oxford University Press, New York, 1999) p. 73.

[34] D. Niedzialek, I. Duchemin, T. B. de Queiroz, S. Osella, A. Rao, R. Friend, X. Blase, S. Kümmel, and D. Beljonne, Adv. Funct. Mater. **25**, 1972 (2015).

[35] R. Österbacka, C. P. An, X. M. Jiang, and Z. V. Vardeny, Science **287**, 839 (2000).

[36] H. Aarnio, M. Westerling, R. Österbacka, M. Svensson, M. R. Andersson, and H. Stubb, Chem. Phys. **321**, 127 (2006).

[37] D. Beljonne, J. Cornil, H. Sirringhaus, P. J. Brown, M. Shkunov, R. H. Friend, and J. L. Brédas, Adv. Funct. Mater. **11**, 229 (2001).

[38] P. Langevin, Ann. Chim. Phys. **28**, 433 (1903).

[39] C. Deibel, A. Baumann, and V. Dyakonov, Appl. Phys. Lett. **93**, 163303 (2008).

[40] A. Pivrikas, G. Juška, A. J. Mozer, M. Scharber, K. Arlauskas, N. S. Sariciftci, H. Stubb, and R. Österbacka, Phys. Rev. Lett. **94**, 176806 (2005).

[41] D. H. K. Murthy, A. Melianas, Z. Tang, G. Juška, K. Arlauskas, F. Zhang, L. D. A. Siebbeles, O. Inganäs, and T. J. Savenije, Adv. Funct. Mater. **23**, 4262 (2013).

[42] G. Juška, K. Genevičius, N. Nekrašas, G. Sliaužys, and R. Österbacka, Appl. Phys. Lett. **95**, 013303 (2009).

[43] G. Juška, K. Genevičius, N. Nekrašas, and G. Sliaužys, Phys. Status Solidi C **7**, 980 (2010).

[44] M. Nyman, O. J. Sandberg, and R. Österbacka, Adv. Energy Mater. **5**, 1400890 (2015).

[45] M. Westerling, R. Österbacka, and H. Stubb, Phys. Rev. B **66**, 165220 (2002).

[46] T. Kirchartz, B. E. Pieters, J. Kirkpatrick, U. Rau, and J. Nelson, Phys. Rev. B **83**, 115209 (2011).

[47] T. Kirchartz and J. Nelson, Phys. Rev. B **86**, 165201 (2012).

[48] N. M. Wilson, *Inverkan Av Indirekt Rekombination På Fotoinducerad Absorption* (in Swedish), M. Sc. Thesis, Åbo Akademi University, 2015.

[49] N. M. Wilson, S. Sandén, O. J. Sandberg, and R. Österbacka, J. Appl. Phys. **121**, 095701 (2017).

[50] O. J. Sandberg, M. Nyman, and R. Österbacka, Phys. Rev. Appl. **1**, 024003 (2014).

[51] O. J. Sandberg, A. Sundqvist, M. Nyman, and R. Österbacka, Phys. Rev. Appl. **5**, 044005 (2016).

[52] A. Sundqvist, O. J. Sandberg, M. Nyman, J.-H. Smått, and R. Österbacka, Adv. Energy Mater. **6**, 1502265 (2016).

[53] A. Wagenpfahl, D. Rauh, M. Binder, C. Deibel, and V. Dyakonov, Phys. Rev. B **82**, 115306 (2010).

[54] J. Hwang, A. Wan, and A. Kahn, Mater. Sci. Eng. R **64**, 1 (2009).

[55] S. Braun, W. R. Salaneck, and M. Fahlman, Adv. Mater. **21**, 1450 (2009).

[56] S. Braun, X. Liu, W. R. Salaneck, and M. Fahlman, Org. Electron. **11**, 212 (2010).

[57] G. Brocks, D. Cakir, M. Bokdam, M. P. de Jong, and M. Fahlman, Org. Electron. **13**, 1793 (2012).

[58] M. Fahlman, A. Crispin, X. Crispin, S. K. M. Henze, M. P. de Jong, W. Osikowicz, C. Tengstedt, and W. R. Salaneck, J. Phys. Condens. Matter **19**, 183202 (2007).

[59] H. Aarnio, P. Sehati, S. Braun, M. Nyman, M. P. de Jong, M. Fahlman, and R. Österbacka, Adv. Energy Mater. **1**, 792 (2011).

[60] Q. Bao, O. Sandberg, D. Dagnelund, S. Sandén, S. Braun, H. Aarnio, X. Liu, W. M. W. M. Chen, R. Österbacka, and M. Fahlman, Adv. Funct. Mater. **24**, 6309 (2014).

[61] G. Juska, K. Arlauskas, M. Viliunas, and J. Kocka, Phys. Rev. Lett. **84**, 4946 (2000).

[62] G. Juška, N. Nekrašas, K. Genevičius, J. Stuchlik, and J. Kočka, Thin Solid Films **451–452**, 290 (2004).

[63] G. Juška, K. Arlauskas, J. Stuchlik, and R. Österbacka, J. Non. Cryst. Solids **352**, 1167 (2006).

[64] G. Juska, K. Arlauskas, M. Viliunas, K. Genevičius, R. Österbacka, and H. Stubb, Phys. Rev. B **62**, R16235 (2000).

[65] G. Juška, K. Genevičius, R. Österbacka, K. Arlauskas, T. Kreouzis, D. D. C. Bradley, and H. Stubb, Phys. Rev. B **67**, 081201 (2003).

[66] R. Österbacka, A. Pivrikas, G. Juška, K. Genevičius, K. Arlauskas, and H. Stubb, Curr. Appl. Phys. **4**, 534 (2004).

[67] A. J. Mozer, N. S. Sariciftci, L. Lutsen, D. Vanderzande, R. Österbacka, M. Westerling, and G. Juška, Appl. Phys. Lett. **86**, 112104 (2005).

[68] A. J. Mozer, G. Dennler, N. S. Sariciftci, M. Westerling, A. Pivrikas, R. Österbacka, and G. Juška, Phys. Rev. B **72**, 035217 (2005).

[69] G. Sliaužys, G. Juška, K. Arlauskas, A. Pivrikas, R. Österbacka, M. Scharber, A. Mozer, and N. S. Sariciftci, Thin Solid Films **511–512**, 224 (2006).

[70] A. Pivrikas, *Charge Carrier Transport and Recombination in Bulk-Heterojunction Solar-Cells*, Ph. D. Thesis, Åbo Akademi University, 2006.

[71] G. Juška, N. Nekrašas, and K. Genevičius, J. Non. Cryst. Solids **358**, 748 (2012).

[72] G. Juška, N. Nekrašas, K. Genevičius, and A. Pivrikas, Appl. Phys. Lett. **102**, 163306 (2013).

[73] A. Armin, G. Juska, M. Ullah, M. Velusamy, P. L. Burn, P. Meredith, and A. Pivrikas, Adv. Energy Mater. **4**, 1300954 (2014).

[74] G. Juška, N. Nekrašas, K. Genevičius, and T. Grigaitis, J. Appl. Phys. **116**, 023702 (2014).

[75] O. J. Sandberg, M. Nyman, S. Dahlström, S. Sandén, B. Törngren, J.-H. Smått, and R. Österbacka, Appl. Phys. Lett. **110**, 153504 (2017).

[76] J. Važgėla, K. Genevičius, and G. Juška, Chem. Phys. **478**, 126 (2016).

[77] J. Peng, X. Chen, O. J. Sandberg, R. Österbacka, and Z. Liang, Adv. Electron. Mater. **2**, 1500333 (2016).

[78] O. J. Sandberg, M. Nyman, and R. Österbacka, Org. Electron. **15**, 3413 (2014).

[79] C. Deibel, Phys. Status Solidi A **206**, 2731 (2009).

[80] S. Bange, M. Schubert, and D. Neher, Phys. Rev. B **81**, 035209 (2010).

[81] J. Lorrmann, B. H. Badada, O. Inganäs, V. Dyakonov, and C. Deibel, J. Appl. Phys. **108**, 113705 (2010).

[82] G. Juška, N. Nekrašas, V. Valentinavicius, P. Meredith, and A. Pivrikas, Phys. Rev. B **84**, 155202 (2011).

[83] G. Juška, K. Genevičius, N. Nekrašas, G. Sliaužys, and G. Dennler, Appl. Phys. Lett. **93**, 143303 (2008).

[84] L. J. A. Koster, E. C. P. Smits, V. D. Mihailetchi, and P. W. M. Blom, Phys. Rev. B **72**, 085205 (2005).

[85] J. C. Scott and G. G. Malliaras, Chem. Phys. Lett. **299**, 115 (1999).

[86] S. Lacic and O. Inganäs, J. Appl. Phys. **97**, 124901 (2005).

[87] Z. V. Vardeny and X. Wei, *Optical Probes of Photoexcitations in Conjugated Polymers*, in: T. A. Skotheim. R. L. Elsenbaumer, J. R. Reynolds (Eds), *Handbook of Conducting Polymers* (Marcel Dekker Inc., New York, 1998) p. 641-647.

[88] H. Aarnio, *Photoexcitation Dynamics in Organic Solar Cell Donor / Acceptor Systems*, Ph. D. Thesis, Åbo Akademi University, 2012.

[89] M. Westerling, C. Vijila, R. Österbacka, and H. Stubb, Chem. Phys. **286**, 315 (2003).

[90] M. Westerling, C. Vijila, R. Österbacka, and H. Stubb, Phys. Rev. B **67**, 195201 (2003).

[91] M. Westerling, C. Vijila, R. Österbacka, and H. Stubb, Phys. Rev. B **69**, 245201 (2004).

[92] O. Epshtein, G. Nakhmanovich, Y. Eichen, and E. Ehrenfreund, Phys. Rev. B **63**, 125206 (2001).

[93] O. Epshtein, Y. Eichen, E. Ehrenfreund, M. Wohlgenannt, and Z. V Vardeny, Phys. Rev. Lett. **90**, 046804 (2003).

[94] R. Metzler and J. Klafter, J. Non. Cryst. Solids **305**, 81 (2002).

[95] A. C. Arango, L. R. Johnson, V. N. Bliznyuk, Z. Schlesinger, S. A. Carter, and H.-H. Hörhold, Adv. Mater. **12**, 1689 (2000).

[96] H.-J. Koo, S. T. Chang, J. M. Slocik, R. R. Naik, and O. D. Velev, J. Mater. Chem. **21**, 72 (2011).

[97] A. Hayakawa, O. Yoshikawa, T. Fujieda, K. Uehara, and S. Yoshikawa, Appl. Phys. Lett. **90**, 163517 (2007).

[98] S. H. Park, A. Roy, S. Beaupré, S. Cho, N. Coates, J. S. Moon, D. Moses, M. Leclerc, K. Lee, and A. J. Heeger, Nat. Photonics **3**, 297 (2009).

[99] N. Nekrašas, K. Genevičius, M. Viliunas, and G. Juška, Chem. Phys. **404**, 56 (2012).

[100] A. Armin, M. Velusamy, P. L. Burn, P. Meredith, and A. Pivrikas, Appl. Phys. Lett. **101**, 083306 (2012).

[101] O. J. Sandberg, S. Sandén, A. Sundqvist, J.-H. J.-H. Smått, and R. Österbacka, Phys. Rev. Lett. **118**, 076601 (2017).

[102] H. Schmidt, K. Zilberberg, S. Schmale, H. Flügge, T. Riedl, and W. Kowalsky, Appl. Phys. Lett. **96**, 243305 (2010).

[103] J. Kim, G. Kim, Y. Choi, J. Lee, S. H. Park, and K. Lee, J. Appl. Phys. **111**, 114511 (2012).

[104] B. Ecker, H.-J. Egelhaaf, R. Steim, J. Parisi, and E. von Hauff, J. Phys. Chem. C **116**, 16333 (2012).

[105] Z. Lin, C. Jiang, C. Zhu, and J. Zhang, ACS Appl. Mater. Interfaces **5**, 713 (2013).

[106] H. Aarnio, M. Westerling, R. Österbacka, M. Svensson, M. R. Andersson, T. Pascher, J. Pan, V. Sundström, and H. Stubb, Synth. Met. **155**, 299 (2005).

[107] T. Tromholt, M. V. Madsen, and F. C. Krebs, Appl. Phys. Lett. **102**, 123904 (2013).

[108] G.-J. A. H. Wetzelaer, M. Kuik, and P. W. M. Blom, Adv. Energy Mater. **2**, 1232 (2012).

[109] T. Kirchartz, F. Deledalle, P. S. Tuladhar, J. R. Durrant, and J. Nelson, J. Phys. Chem. Lett. **4**, 2371 (2013).

[110] F. Deledalle, P. S. Tuladhar, J. Nelson, J. R. Durrant, and T. Kirchartz, J. Phys. Chem. C **118**, 8837 (2014).

[111] Z.-L. Guan, J. B. Kim, H. Wang, C. Jaye, D. A. Fischer, Y.-L. Loo, and A. Kahn, Org. Electron. **11**, 1779 (2010).

[112] Z. L. Guan, J. B. Kim, Y.-L. Loo, and A. Kahn, J. Appl. Phys. **110**, 43719 (2011).

[113] Z. Xu, L.-M. Chen, M.-H. Chen, G. Li, and Y. Yang, Appl. Phys. Lett. **95**, 013301 (2009).

[114] T. Drori, J. Holt, and Z. V. Vardeny, Phys. Rev. B **82**, 075207 (2010).

[115] S. Singh, B. Pandit, G. Hukic-Markosian, T. P. Basel, Z. V. Vardeny, S. Li, and D. Laird, J. Appl. Phys. **112**, 123505 (2012).

[116] J. Guo, H. Ohkita, S. Yokoya, H. Benten, and S. Ito, J. Am. Chem. Soc. **132**, 9631 (2010).

[117] G. Zhang, T. M. Clarke, and A. J. Mozer, J. Phys. Chem. C **120**, 7033 (2016).

[118] Y.-H. Lin, Y.-T. Tsai, C.-C. Wu, C.-H. Tsai, C.-H. Chiang, H.-F. Hsu, J.-J. Lee, and C.-Y. Cheng, Org. Electron. **13**, 2333 (2012).

[119] S. Venkatesan, J. Chen, E. C. Ngo, A. Dubey, D. Khatiwada, C. Zhang, and Q. Qiao, Nano Energy **12**, 457 (2015).

[120] E. Wang, J. Bergqvist, K. Vandewal, Z. Ma, L. Hou, A. Lundin, S. Himmelberger, A. Salleo, C. Müller, O. Inganäs, F. Zhang, and M. R. Andersson, Adv. Energy Mater. **3**, 806 (2013).

[121] E. Wang, L. Hou, Z. Wang, S. Hellström, F. Zhang, O. Inganäs, and M. R. Andersson, Adv. Mater. **22**, 5240 (2010).

[122] S. Shao, J. Liu, J. Bergqvist, S. Shi, C. Veit, U. Würfel, Z. Xie, and F. Zhang, Adv. Energy Mater. **3**, 349 (2013).

[123] M. Nyman, O. J. Sandberg, and R. Österbacka, Synth. Met. **201**, 6 (2015).

[124] D. A. Vithanage, E. Wang, Z. Wang, F. Ma, O. Inganäs, M. R. Andersson, A. Yartsev, V. Sundström, and T. Pascher, Adv. Energy Mater. **4**, 1301706 (2014).

[125] Z. Tang, W. Tress, Q. Bao, M. J. Jafari, J. Bergqvist, T. Ederth, M. R. Andersson, and O. Inganäs, Adv. Energy Mater. **4**, 1400643 (2014).

[126] J. Bergqvist, C. Lindqvist, O. Bäcke, Z. Ma, Z. Tang, W. Tress, S. Gustafsson, E. Wang, E. Olsson, M. R. Andersson, O. Inganäs, and C. Müller, J. Mater. Chem. A **2**, 6146 (2014).

[127] R. Kroon, R. Gehlhaar, T. T. Steckler, P. Henriksson, C. Müller, J. Bergqvist, A. Hadipour, P. Heremans, and M. R. Andersson, Sol. Energy Mater. Sol. Cells **105**, 280 (2012).

ISBN 978-952-12-3667-9